Nano Energy 77 (2020) 105309

Contents lists available at ScienceDirect

Nano Energy

journal homepage: http://www.elsevier.com/locate/nanoen

Inorganic narrow bandgap $CsPb_{0.4}Sn_{0.6}I_{2.4}Br_{0.6}$ perovskite solar cells with exceptional efficiency

Seojun Lee [a,1], Janghyuk Moon [a,1], Jun Ryu [a], Bhaskar Parida [a], Saemon Yoon [a], Dong-Gun Lee [a], Jung Sang Cho [b,*], Shuzi Hayase [c,**], Dong-Won Kang [a,***]

[a] School of Energy Systems Engineering, Chung-Ang University, Seoul, 06974, Republic of Korea
[b] Department of Engineering Chemistry, Chungbuk National University, Cheongju, 28644, Republic of Korea
[c] Info-Powered Energy System Research Center, The University of Electro-Communications, 1-5-1 Chofugaoka, Chofu, Tokyo, 182-8585, Japan

ARTICLE INFO

Keywords:
Inorganic perovskite
Bandgap
Solar cells
Stability

ABSTRACT

The instability of organic/inorganic hybrid perovskite solar cells (PSCs) has motivated the development of the inorganic halide PSCs. However, the representative inorganic $CsPbI_3$ still suffers from phase instability in ambient air and an unfavorable wide bandgap (1.75 eV), thereby limiting its efficiency. In this study, a binary metal composition of Pb:Sn = 4:6 in $CsPb_{1-x}Sn_xI_3$ is found to stabilize the cubic $CsPbI_3$ phase and reduce its bandgap. Based on the parental $CsPb_{0.4}Sn_{0.6}I_3$, compositional engineering is further conducted for $CsPb_{0.4}Sn_{0.6}I_{3-y}Br_y$ perovskites. After introducing a suitable Br content (y = 0.6), there are remarkable improvements in the crystalline quality and a denser morphology in the perovskite films. Furthermore, in the novel inorganic $CsPb_{0.4}Sn_{0.6}I_{2.4}Br_{0.6}$ perovskite, trap-assisted recombination is effectively suppressed, with a desirable narrow bandgap of 1.35 eV. As a result, the corresponding PSC delivered an unprecedented efficiency of 12.34%, which is the highest among the inorganic Sn-rich (Sn > 50%) PSCs reported to date. Additionally, the unencapsulated PSC demonstrates impressive long-term air stability, which exceeds the performance of 100% Pb-based inorganic $CsPbI_3$ and/or $CsPbI_2Br$ PSCs reported. This near-infrared absorbing (~930 nm) inorganic PSC with exceptional efficiency, durability and Pb-reduction generates a promising route for further progress of perovskite-based photovoltaics.

1. Introduction

Organic-inorganic hybrid (OIH) perovskite solar cells (PSCs) have attracted great research interest in recent years due to their high power conversion efficiency (PCE). The outstanding properties of OIH PSCs, such as low fabrication cost, high absorption coefficient, high carrier mobilities, and long carrier diffusion lengths lead to a rapid increase in their PCE to 25.2%, which is comparable to silicon solar cells. However, several issues remain before the commercialization of these PSCs, especially the low reliability and the use of toxic lead (Pb) [1–4]. To improve the reliability, recent studies report that the A site of perovskite (ABX_3), such as methylammonium (MA^+) and formamidinium (FA^+), can be replaced by inorganic cations such as cesium (Cs^+) [5–9]. Hence, the inorganic PSCs using $CsPbI_{3-x}Br_x$ (x = 0–3) have been widely investigated. Nevertheless, when the Br content is low, those inorganic PSCs are unstable under air ambient condition [10–12]. In addition to the toxicity of Pb, Pb-based inorganic perovskites exhibit bandgaps of 1.7–2.3 eV, which are much wider than the preferred values (1.2–1.4 eV) for single junction from the Shockley-Queisser limit [13]. Several studies have tried to replace the Pb by Sn to produce Sn-based inorganic PSCs, although their PCE (3–4.8%) and stability are far below the Pb-based ones [14–17]. Using the binary metal approach, lead-free $CsSn_{0.5}Ge_{0.5}I_3$ PSCs using germanium (Ge) were fabricated, but the PCE was still limited to 7.1% [18]. In comparison, the Pb–Sn binary PSCs have delivered better performance, even though they are still based on the Pb-rich (50–60%) material [19,20]. Overall, there remains the need to find perovskite absorbers that simultaneously display high PCE, good stability, reduced Pb content, and narrow bandgap. In this study, we

* Corresponding author.
** Corresponding author.
*** Corresponding author.
E-mail addresses: jscho@chungbuk.ac.kr (J.S. Cho), hayase@uec.ac.jp (S. Hayase), kangdwn@cau.ac.kr (D.-W. Kang).
[1] These authors contributed equally to this work.

https://doi.org/10.1016/j.nanoen.2020.105309
Received 18 May 2020; Received in revised form 21 July 2020; Accepted 19 August 2020
Available online 26 August 2020

report such an inorganic perovskite absorber with a narrow bandgap of 1.35 eV. First, $CsPb_{1-x}Sn_xI_3$ perovskites were thoroughly investigated using density functional theory (DFT) calculation, in order to find the desirable Pb:Sn ratio displaying improved phase stability at low Pb content. Additional experiments confirmed that the most stable phase occurs at 60% Sn. Based on this low-Pb (Sn-rich) absorber, we further employed a mixed halide approach by introducing bromine (Br) to form $CsPb_{0.4}Sn_{0.6}I_{3-y}Br_y$ (y = 0.0–1.0) perovskites. When y = 0.6, the material had better crystallinity and stability than the parent compound ($CsPb_{0.4}Sn_{0.6}I_3$) while also showing fewer pinholes in the film surface. Moreover, photoluminescence (PL) study indicated that non-radiative recombination was suppressed by incorporating Br. In addition, the electronic impedance spectra exhibited improved recombination resistance with Br addition when the device was prepared with an inverted planar architecture. In photovoltaic characterization experiments under 1 sun, the $CsPb_{0.4}Sn_{0.6}I_{3-y}Br_y$ PSC with y = 0.6 had an impressive PCE of 12.34%, which is better than all other reported inorganic Sn-rich (Sn > 50%) PSCs. Furthermore, this PSC exhibited remarkable long-term stability in the air at RH 30–70%. Over 70% of its initial PCE was retained after 30 days without any encapsulation, whereas devices based on $CsPbI_3$ and $CsPb_{0.4}Sn_{0.6}I_3$ degraded completely during this period. Based on these experimental results, we believe that our approach made significant contribution to developing highly stable, efficient, and Pb-reduced photovoltaics for inorganic Pb–Sn PSCs. $CsPb_{0.4}Sn_{0.6}I_{2.4}Br_{0.6}$ with a narrow gap of 1.35 eV can also be used in the near-infrared (NIR) absorbing sub-cell of perovskite-perovskite tandem photovoltaics.

2. Experimental section

2.1. Materials

Cesium iodide (CsI, 99.999%, Alfa Aesar), lead iodide (PbI_2, 99.9985%, Alfa Aesar), lead bromide ($PbBr_2$, 99.999%, Alfa Aesar), tin iodide (SnI_2, 99.999%, Alfa Aesar), tin bromide ($SnBr_2$, 99.2%, Alfa Aesar), and tin fluoride (SnF_2, 99%, Sigma-Aldrich) were purchased and used as precursors for the inorganic Sn-rich perovskites. Dimethylformamide (DMF, 99.5%, Samchun Chemical) and dimethyl sulfoxide (DMSO, 99.8%, Samchun Chemical) were used as solvents.

The $CsPbI_3$ perovskite precursor solution was prepared by dissolving an equimolar ratio of PbI_2 (0.8 M) and CsI (0.8 M) in a mixed solvent of (4:1) DMF:DMSO. And, the 0.5 M $CsPb_{1-x}Sn_xI_3$ precursor solutions were prepared with $CsI:PbI_2:SnI_2$ = 1.0:1-x:x (x = 0.2, 0.4, 0.6, 0.8, 1.0) and 10 mol% of SnF_2 for each conditions. Also, 0.5 M $CsPb_{0.4}Sn_{0.6}I_{3-y}Br_y$ precursor solutions were prepared with $CsI:PbI_2:PbBr_2:SnI_2$ = 1.0:0.4–0.5y:0.5y:0.6 (y = 0, 0.3, 0.6) and $CsI:PbBr_2:SnI_2:SnBr_2$ = 1.0:0.4:0.5:0.1 (y = 1.0), and 10 mol% of SnF_2 for each conditions by dissolving them in a mixed solvent of (1:1) DMF:DMSO. All precursor solutions were stirred at 60°C overnight.

2.2. Device fabrication

Indium tin oxide (ITO) substrates were cleaned sequentially with acetone, methanol, and isopropanol by sonification for 15 min in each step. After drying in an oven, the substrates were treated with ultraviolet-ozone for 20 min prior to use. To form the hole transport layer (HTL), poly(3,4-ethylenedioxythiophene) polystyrenesulfonate (PEDOT:PSS, PVP AI 4083) was spin-coated onto the substrates at 4000 rpm for 50 s and annealed at 150 °C for 20 min. The DMSO treatment was performed by dropping 200 μL of DMSO onto each PEDOT:PSS film during the spin coating. They were then dried again at 150 °C. The substrates coated with PEDOT:PSS were then transferred into a N_2 glove box. The perovskite precursor solution was spin-coated at 5000 rpm for 60 s on top of the PEDOT:PSS film, and annealed at 80 °C for 30 min on a hot plate.

For the electron transport layer (ETL), a 20 mg/mL solution of phenyl-C61-butyric acid methyl ester ($PC_{61}BM$, 99.5%) in chlorobenzene (CBZ) was spin-coated onto the perovskite film at 1500 rpm for 35 s. Subsequently, cerium (III) acetylacetonate hydrate (CeO_x, 0.5 mg/mL in isopropanol) was spin-coated onto the $PC_{61}BM$ film at 6000 rpm for 30 s. After annealing the layers at 80 °C for 10 min on a hot plate, silver (Ag) electrodes were thermally evaporated under high vacuum ($<1 \times 10^{-6}$ Torr) with a shadow mask (4 mm^2). The 50 devices were made for each perovskite composition to get statistical evaluation.

2.3. Perovskite film characterization

Crystalline structures of the perovskite films were examined by X-ray diffraction (XRD; New D8-Advance, Bruker-AXS). X-ray photoelectron spectroscopy (XPS) measurement was performed with a K-Alpha + system (Thermo Fisher Scientific) using monochromatic Al Kα irradiation (1486.6 eV). The surface morphologies and energy dispersive X-ray spectroscopy (EDS) analyses were investigated by field emission scanning electron microscopy (FE-SEM; AURIGA, Carl Zeiss). The optical absorption spectra were characterized by ultraviolet–visible (UV–Vis) spectroscopy (UV-2700, Shimadzu). Both the steady-state and time-resolved photoluminescence (PL) measurements of the fabricated perovskite films were conducted using a spectrofluorometer (Fluorolog3 with TCSPC, HORIBA SCIENTIFIC) with a laser excitation wavelength of 374 nm. Ultraviolet photoelectron spectroscopy (UPS) measurement was performed with XPS-Theta Probe (Thermo Fisher Scientific) and Al Kα radiation (1486.6 eV). The carrier concentration and mobility were characterized using a Hall effect measurement system (HEM-3000, ECOPIA).

2.4. Device characterization

All device characterizations were carried out in ambient atmosphere. All current-voltage (J-V) curves of the fabricated PSCs were measured using a solar simulator (PEC-L01, Peccell Technologies) under standard AM1.5 illumination (100 mW cm^{-2}) in atmospheric air conditions. To detect the responses as a function of the spectral wavelength, the external quantum efficiency (EQE) spectrum was characterized using a power source (Abet Technologies 150 W xenon lamp, 13014) with a monochromator (DongWoo Optron, MonoRa500i) and a CompactStat instrument (Ivium Technologies; Eindhoven, The Netherlands). The electrochemical impedance spectroscopy (EIS) analysis used an impedance analyzer (Solartron 1287) in the dark, in the frequency range from 1 kHz to 1 MHz with a perturbation amplitude of 0.01 V.

2.5. DFT calculations

All density functional theory (DFT) calculations were performed using projector-augmented wave pseudopotentials implemented in the Vienna ab initio simulation package (VASP) [21–24]. For the exchange-correlation functional, the generalized gradient approximation (GGA) with Perdew-Burke-Ernzerhof (PBE) functional was employed. In the standard computational parameters, a k-point mesh in the Monkhorst-Pack scheme was set at 8 × 8 × 8 for the unit cell and 3 × 3 × 3 for the 2 × 2 × 2 supercell of cubic perovskite. All internal atomic coordinates and lattice vector were fully relaxed until the force on each atom was less than 0.01 eV $Å^{-1}$, with the energy cut-off of 500 eV for the planewave basis points. To observe the local charge and calculate the net charge, Bader charge analysis was performed [25].

3. Results and discussion

Prior to this study, an inorganic PSC using $CsPbI_3$ as absorber has the highest PCE (~18%) among inorganic $CsPbX_3$ perovskites, thanks to it's a relatively lower bandgap (1.73 eV) than other Br-added counterparts such as $CsPbI_2Br$ (1.9 eV), $CsPbIBr_2$ (2.03 eV), and $CsPbBr_3$ (2.3 eV). Hence, a lower bandgap generally allows for higher short circuit current density (J_{sc}), which is beneficial for such a high efficiency. As mentioned

earlier, some issues remain regarding the content of toxic Pb and the quick degradation from the α (3D perovskite) to δ (non-perovskite) phase under air ambience [12,26,27]. To design a more stable and environmentally friendly light harvester, we systematically investigated the Pb–Sn binary composition in inorganic perovskites. First, we used the tolerance factor (Goldschmidt) and the formation energy of $CsPb_{1-x}Sn_xI_3$ perovskites in the range of x = 0.0–1.0 to represent the geometric stability of the materials [28–32]. The geometric tolerance factor (*T*) is defined as follows:

$$T = \frac{R_A + R_x}{\sqrt{2}(R_B + R_x)} \quad (1)$$

where R_A, R_B, and R_X are the radii of the cation A (Cs^+: 1.67 Å), divalent metal ion B (Pb^{2+}: 1.19 Å, Sn^{2+}: 0.93 Å), and the anion (I^-: 2.20 Å), respectively [33]. Because Sn^{2+} is smaller than Pb^{2+}, *T* increases as more Sn is introduced into the system. In Fig. 1a, the calculated *T* gradually increases from 0.807 to 0.875 when the Sn content (x) increases from 0 to 1.0. This means that Pb replacement by Sn enhances the stability of the perovskite structure. It has been also reported that the Sn–I bond length is shorter than that of Pb–I, also contributing to the formation of a more stable perovskite lattice [34].

The stability of the perovskites was also evaluated by the formation energy (enthalpy, ΔH) defined in the following formula:

$$\Delta E_f = E(CsPb_{1-x}Sn_xI_3) - [(1-x)E(CsPbI_3) + xE(CsSnI_3)] \quad (2)$$

where $E(CsPbI_3)$and $E(CsSnI_3)$are the total free energies for cubic perovskites of $CsPbI_3$ and $CsSnI_3$, respectively. All 128 possible configurations of $CsPb_{1-x}Sn_xI_3$ in 2 × 2 × 2 supercell of cubic perovskite were calculated, and the minimum energy structures were identified and illustrated in Fig. S1 of Supporting Information. Note that there are several intermediate phases with different Sn configurations but similar energies, implying that various local configurations with similar stability can coexist as a mixture. When the ratio of Sn substitution increased from 0 to 0.5, the formation energy continued to decrease, implying a more stable intermediate phase in this composition range. However, when x > 0.625, the formation energy gradually increased to indicate a reduced stability. This phenomenon has been attributed to the mismatched ionic radii of Pb^{2+} and Sn^{2+} or a significant change in the electron affinity [35]. Therefore, these inorganic $CsPb_{1-x}Sn_xI_3$ perovskites are the most stable in the region of x = 0.5–0.6. Fig. 1b presents the cubic crystal structures of the inorganic perovskites with the general formula ABX_3 (A = Cs^+, B = Pb^{2+}, Sn^{2+}, and X = I^-). $CsPbI_3$ and $CsPb_{0.375}Sn_{0.625}I_3$ perovskites are presented as representative examples here, and the crystal structures with different Sn ratios are presented in Fig. S1. The simulated crystal structures illustrate that Pb exchanges with Sn at the B cation site of the cubic perovskite. The Pb–I binding energy in the BI_6 octahedral structure is expected to be higher than that of Sn–I, due to the stronger electron transfer from Pb to I. Pb and Sn share the edge of I atom as the Sn substitution increases. As the difference in electric charge transfer increases, the Coulomb interaction also increases, which means a decreasing thermodynamic stability. To reduce this effect, solid solutions are expected to form depending on the cations. The most stable structure has Pb–I–Sn bonding configurations, whereas it is less stable with increasing formation of Sn–I–Sn or Pb–I–Pb. To experimentally verify the simulation results, we measured the X-ray diffraction (XRD) patterns to examine the phase stability of fabricated $CsPb_{1-x}Sn_xI_3$ perovskite films in highly humid air (RH: 70–80%), as shown in Fig. 1c, d, and Fig. S2. All tested samples initially exhibited cubic main peaks of (100) and (200) without structural modification. The pristine $CsPbI_3$ was degraded quickly from α (3D perovskite) to δ (non-perovskite) phase within 1 h, in agreement with previous studies

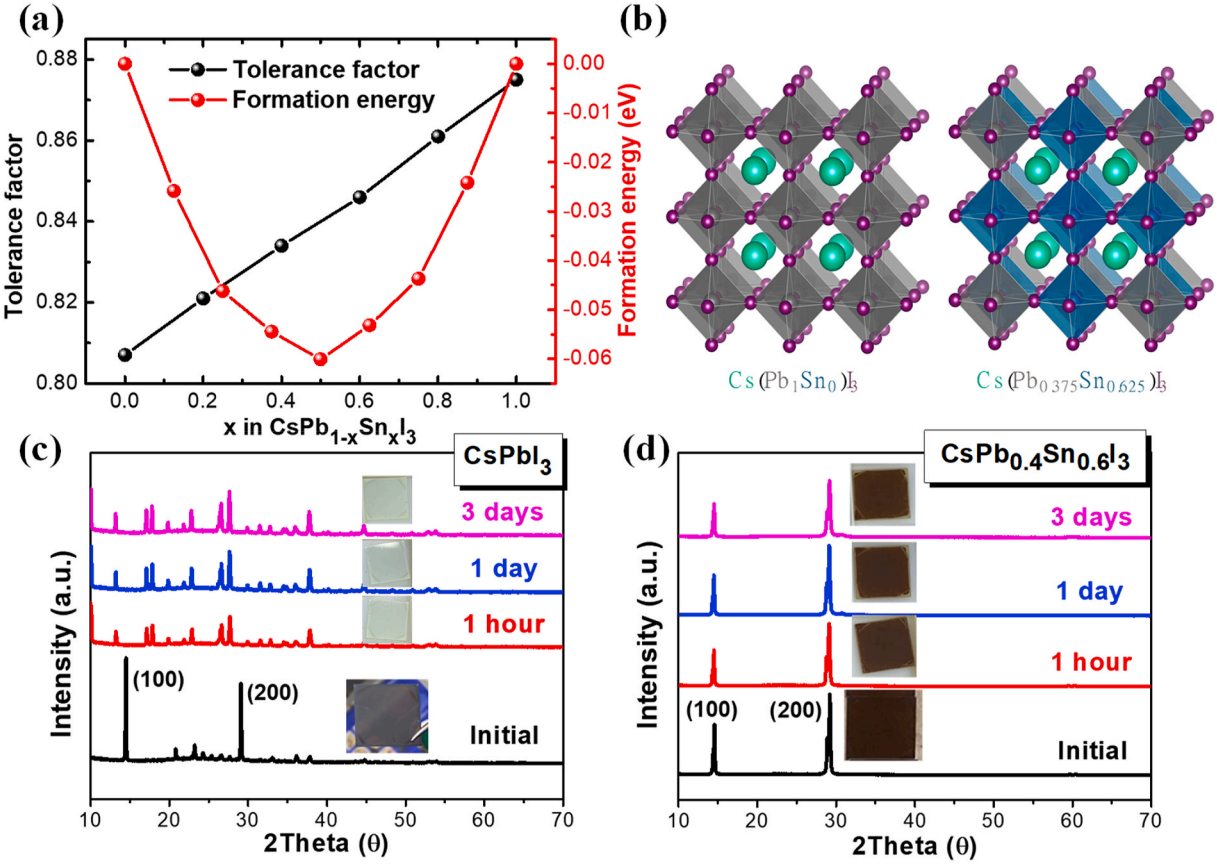

Fig. 1. (a) Calculated tolerance factors and formation energy of $CsPb_{1-x}Sn_xI_3$ as function of x. (b) Schematic crystal structures of $CsPbI_3$ and $CsPb_{0.375}Sn_{0.625}I_3$. Time-dependent XRD patterns of (c) $CsPbI_3$ and (d) $CsPb_{0.4}Sn_{0.6}I_3$ perovskite films at RH = 70–80%.

on the atmospheric instability of $CsPbI_3$ [36–38]. In Fig. S2, the $CsPb_{0.8}Sn_{0.2}I_3$ (x = 0.2) film was also degraded to a similar level. When x = 0.4, the deterioration was slightly less, and the film with x = 0.6 was not degraded at all after 3 days in the highly humid air. However, when x > 0.8, the principal diffraction peaks gradually decreased, and peaks of degradation products (31°) were additionally observed after aging [33]. This observation agrees with the above theoretical study and may be related to the increase in the formation energy. Based on these results, $CsPb_{1-x}Sn_xI_3$ (x = 0.6) perovskite was further investigated due to its best phase stability compared to $CsPbI_3$. In addition, we calculated the density of states (DOS) of the $CsPb_{1-x}Sn_xI_3$ perovskites using DFT (Fig. S3a). Fig. S3b plots the calculated bandgap, which decreased from 1.59 to 0.62 eV with increasing x. This is in good agreement with previous computational/experimental results [30,39]. The projected DOS of $CsPbI_3$ shows that the valence band maximum (VBM) mainly consists of the Sn *s* state and the Pb *p* state, and the conduction band minimum (CBM) is dominated by the Pb *p* state with some of the Sn *p* state. Substitution of Pb^{2+} by Sn^{2+} in the perovskite structure narrows the bandgap by pushing down the CBM, as the occupied p^2 orbitals of Sn^{2+} exhibit a lower energy to couple with the *p* orbitals of I. This suggests the possibility to achieve the desired low bandgap in $CsPb_{1-x}Sn_xI_3$ perovskites with a relatively small value of x. Stabilization of the partially substituted perovskite structure may originate from lattice distortion and charge disproportionation in the substituted system.

The calculated Bader charges (Fig. S3c) show less charge transfer from Sn^{2+} to I^-, which results in a lower CBM and a decreased lattice constant from 12.72 to 12.50 Å. Thus, the $CsPb_{0.4}Sn_{0.6}I_3$ composition appears to be optimal by combining good structural stability and the stability of Sn^{2+} cations. From these results, $CsPb_{0.4}Sn_{0.6}I_3$ might be a promising inorganic perovskite absorber with desirable characteristics such as high phase stability, reduced Pb content, and narrow bandgap.

For further property improvement, additional compositional engineering was carried out by introducing Br into the parent compound $CsPb_{0.4}Sn_{0.6}I_3$, as the I–Br mixed halide is known to be more stable than triiodide [40–43]. The structural properties of $CsPb_{0.4}Sn_{0.6}I_{3-y}Br_y$ perovskites were predicted by DFT simulation. First, the tolerance factor and formation energy were calculated for each Br content, as shown in Fig. 2a and b. As more Br is incorporated (y = 0 to 1.0), the tolerance factor gradually increases from 0.846 to 0.85, and the formation energy gradually becomes negative from y = 0 to y = 0.75. The formation energy can be described as follows:

$$\Delta E_f = E\left(CsPb_{0.375}Sn_{0.625}I_{3-y}Br_y\right) - \left[(1-x)E(CsPb_{0.375}Sn_{0.625}I_3) + xE(CsPb_{0.375}Sn_{0.625}Br_3)\right] \quad (3)$$

where $E(CsPb_{0.375}Sn_{0.625}I_3)$ and $E(CsPb_{0.375}Sn_{0.625}Br_3)$ are the total free energies of the respective cubic perovskites. The ground states of $CsPb_{0.375}Sn_{0.625}I_{3-y}Br_y$ compositions were examined by considering the attractive (repulsive) interactions between Br–Pb(Sn)–Br and the local symmetric configuration in the octahedral structures of B cation (Figs. S4 and S5). The convex hull of $CsPb_{0.375}Sn_{0.625}I_{3-y}Br_y$ indicates

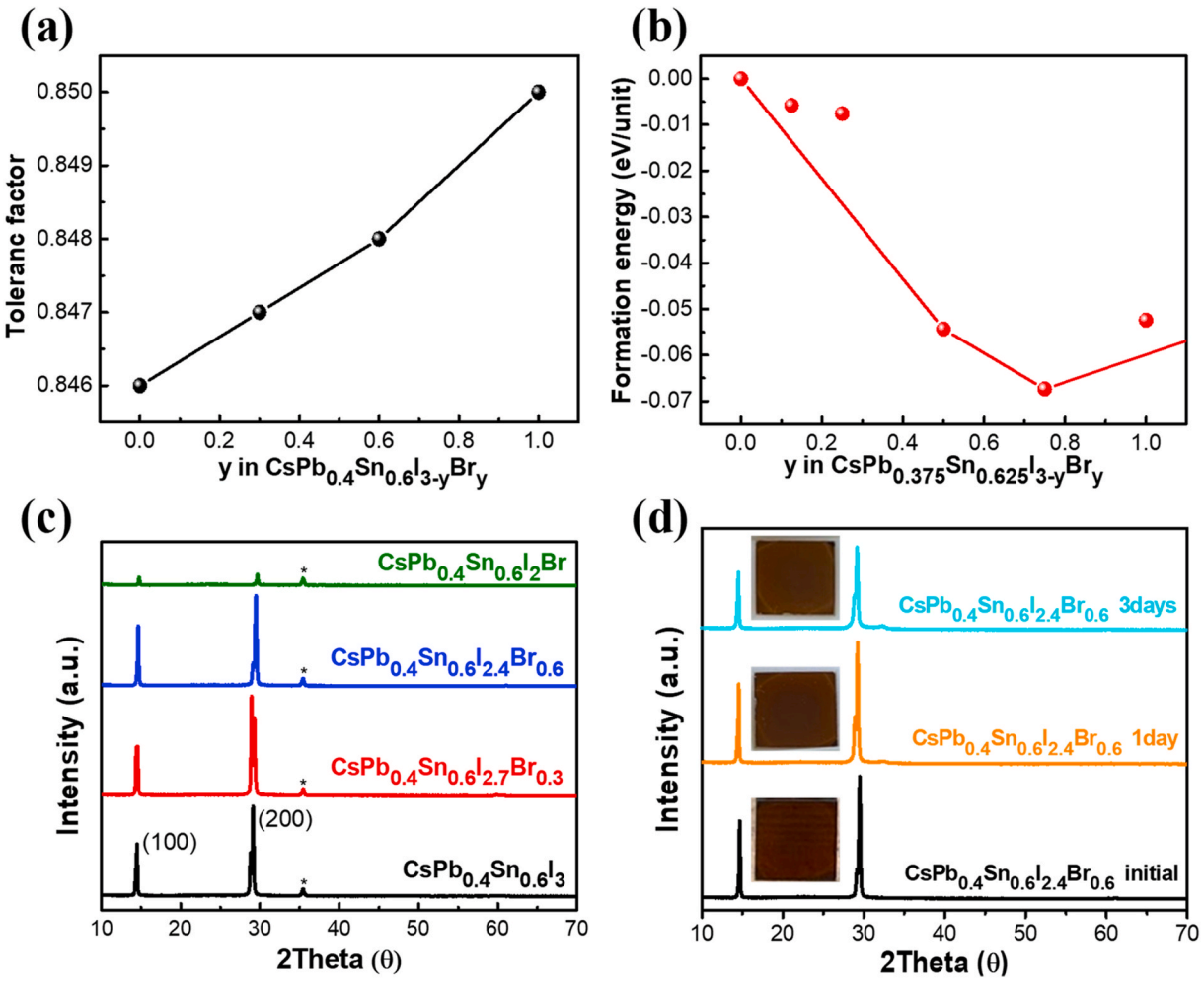

Fig. 2. (a) Calculated tolerance factors of $CsPb_{0.4}Sn_{0.6}I_{3-y}Br_y$ as function of y. (b) Calculated formation energy of $CsPb_{0.375}Sn_{0.625}I_{3-y}Br_y$ as function of y. (c) XRD patterns of the inorganic Sn-rich $CsPb_{0.4}Sn_{0.6}I_{3-y}Br_y$ perovskite films. (* is ITO peak). (d) Time-dependent XRD patterns of $CsPb_{0.4}Sn_{0.6}I_{2.4}Br_{0.6}$ perovskite films at RH = 70–80%.

that there are two intermediate phases: $CsPb_{0.375}Sn_{0.625}I_{2.5}Br_{0.5}$ and $CsPb_{0.375}Sn_{0.625}I_{2.25}Br_{0.75}$. Upon further substitution of I by Br, the Pb $(I–Br)_6$ octahedral structures lose their geometrical symmetry due to structural distortion, which results in thermodynamic instability in the cubic Br-substituted $CsPb_{0.375}Sn_{0.625}I_{3-y}Br_y$. The above results suggest that the crystallinity and stability of $CsPb_{0.4}Sn_{0.6}I_3$ have some further room for improvement. Experimentally, the fabricated $CsPb_{0.4}Sn_{0.6}I_{3-y}Br_y$ perovskite films with various Br contents were characterized by XRD in Fig. 2c.

Like the $CsPb_{0.4}Sn_{0.6}I_3$ perovskite film, the I–Br mixed halide perovskite films also showed only cubic (100) and (200) main peaks without other residual peaks (i.e., no atypical crystalline properties). We have shown the magnified area of (100) and (200) planes in Fig. S6. Interestingly, there is shoulder peaks near (100) and (200) planes, especially in $y = 0$, $y = 0.3$ perovskites. In fact, many studies on $CsSnI_3$ perovskite reported such twin peaks at very similar diffraction angles [14,16,44,45]. From our DFT calculations, the cubic α-phase is relatively unstable when the Br content is low ($y = 0 \sim 0.25$) as displayed in Fig. 2b. Hence, orthorhombic $CsSnI_3$ phase could also be made in the Sn-rich perovskite composition. When the Br content increased over 0.5, on the other hand, the formation energy reduces and the pure cubic phase could dominate. The extracted tolerance factors are also supporting well about these trend (Fig. 2a). It is judged that these theoretical calculations are well connected to the experimental results of the XRD. Additionally, there is a result in which the peak intensity of the orthorhombic $CsSnI_3$ phase was suppressed as Br increases in $CsSnI_{3-x}Br_x$ [46]. This is also similar to our results. On the basis of the interconnection between DFT estimation, XRD, and practical stability tests, it is interpreted that the mixed halide approach using suitable introduction of Br (~0.6) can promote stable cubic α-phase of inorganic Pb–Sn perovskite, which is beneficial for high photovoltaic performance and durability under ambient air. The principal peaks of (100) and (200) gradually shifted from 14.49° to 14.75° and from 29.12° to 29.67°, respectively, as the amount of added Br increased. Thus, the substitution of I^- by Br^- with a smaller ionic radius reduced the perovskite lattice constant. Additionally, the intensity of the principal diffraction peaks increased at a higher Br content ($y = 0.3$ and 0.6), meaning that the incorporation of Br^- forming mixed halides improved the crystallinity of the inorganic Sn-rich $CsPb_{0.4}Sn_{0.6}I_{3-y}Br_y$ perovskite. For more investigation of the crystallinity, we calculated the full width at half maximum (FWHM) and the crystalline sizes in (100) plane for perovskites with different composition based on well-known Scherrer equation, as added in Table S1. The FWHM values of $CsPb_{0.4}Sn_{0.6}I_{3-y}Br_y$ perovskites are 0.14°, 0.14°, 0.12°, and 0.2° for $y = 0$, 0.3, 0.6, and 1.0, respectively. The crystalline sizes are 572.0, 572.3, 667.7, and 407.5 Å for $y = 0$, 0.3, 0.6, and 1.0, respectively, which are good agreement with the intensity of the principal diffraction peaks. However, an excess amount of Br ($y = 1.0$, $CsPb_{0.4}Sn_{0.6}I_2Br$) reduced the diffraction intensity, which is likely attributable to deteriorated crystallinity due to lattice distortion with excess Br. In order to elucidate this, we examined the structural changes of different $CsPb_{0.375}Sn_{0.625}I_{3-y}Br_y$ perovskites (Figs. S4 and S5). Although a constant cubic structure was maintained up to $CsPb_{0.375}Sn_{0.625}I_{2.25}Br_{0.75}$ ($y = 0.75$), the structure with $y = 1.0$ suffered from Jahn-Teller distortion, which could significantly reduce the crystallinity. The substituted Br is preferentially located near the Pb atom than near the Sn atom, because Br becomes a more negative ion than I and thus requires more charge transfer from the cation at B sites. Compared to Sn^{2+}, Pb^{2+} can more easily donate electron to the anion according to the Bader net charge analysis in Fig. S7c. In the supercell of $CsPb_{0.375}Sn_{0.625}I_{2.25}Br_{0.75}$, three Pb atoms are coordinated with six anions (four I, two Br). The two Br are coordinated to Pb in a symmetrical distribution, leading to the formation of ordered octahedra. However, distorted octahedra are expected to form when more Br anions become coordinated. The length of Br–Pb bonds is reduced by strong hybridization because there is more charge transfer than in I–Pb, as shown in Fig. S7c and d. For this reason, it is assumed that the crystallinity of $CsPb_{0.4}Sn_{0.6}I_2Br$ is significantly reduced. This structural distortion would affect the morphological and optical properties of the perovskite films, as will be discussed below. The projected DOS of $CsPb_{0.375}Sn_{0.625}I_{3-y}Br_y$ also shows an increasing bandgap with y (Fig. S7a). In Fig. S7b, when the Br content increases, $CsPb_{0.375}Sn_{0.625}I_{2.25}Br_{0.75}$ has a saturated direct bandgap of 1.20 eV. The electron occupancy of Br *s* state reduces the peak value of VBM, and the more positively charged Pb^{2+} cation pushes the CBM of I and the Br *s* states as shown in Fig. S7c and d. Considering the crystallinity, stability, and bandgap, $CsPb_{0.4}Sn_{0.6}I_{2.4}Br_{0.6}$ ($y = 0.6$) was chosen as the preferred composition in this study. The phase stability of the corresponding perovskite thin film was examined in humid air (RH: 70–80%) by XRD measurement (Fig. 2d). As expected, the XRD patterns showed a very stable phase with no additional degradation peaks. In addition to XRD measurement, we also observed the film stability with different compositions by utilizing absorption and PL measurements in humid air (R.H.:50%), as shown in Fig. S8. The absorption and PL of $CsPbI_3$ perovskite film were completely degraded within 1 day, which is consistent with the XRD pattern. On the other hand, enhanced stability of the perovskite by introducing 60% of Sn at B-site was also confirmed in UV–Vis absorbance and PL analyses. Compared to $CsPbI_3$, substantial amount of absorbance of $CsPb_{0.4}Sn_{0.6}I_3$ was maintained. Also, reduction of PL intensity could be significantly suppressed. Impressively, $CsPb_{0.4}Sn_{0.6}I_{2.4}Br_{0.6}$ perovskite showed more enhanced film stability. In this case, the performance degradation is much limited after aging, which is also consistent with the results from XRD and DFT calculations implemented in the VASP. Enhancement of structural stability by these compositional engineering could allow for practical improvement in durability under ambient air, from our investigation. Besides the structural and optical stability, the surface structure of the light absorber thin film is also important for thin film PSCs. From the field emission scanning electron microscopy (FE-SEM) images in Fig. 3, the incorporation of Br improves not only the crystallinity but also the morphology of the inorganic Sn-rich $CsPb_{0.4}Sn_{0.6}I_{3-y}Br_y$ perovskite films. In Fig. 3a, huge discontinuities and big pinholes were observed on the surface of pristine $CsPb_{0.4}Sn_{0.6}I_3$ film without Br addition. Such a morphology may cause direct contact of the electron transport layer (ETL) and hole transport layer (HTL), which can induce detrimental recombination loss in device operation. As the Br ratio increased, the topography became more continuous, and there were fewer pinholes in Fig. 3b. In Fig. 3c, the $CsPb_{0.4}Sn_{0.6}I_{2.4}Br_{0.6}$ perovskite film showed the most compact and densest morphology among all studied films, thus it could prevent recombination losses and local current drain. This is presumably because Br incorporation passivates the defects in the grain boundary (GB) and improves the crystalline properties in OIH mixed halide perovskites [47]. On the other hand, the $CsPb_{0.4}Sn_{0.6}I_2Br$ perovskite film again displayed discontinuous morphology with more pinholes, and the grain size was remarkably reduced (Fig. 3d). This effect well matches the XRD results in Fig. 2c, and the main cause is considered to be the distortion of crystalline structure (Fig. S5). We have displayed EDS mapping and elemental analyses of the $CsPb_{0.4}Sn_{0.6}I_{3-y}Br_y$ perovskite films in Fig. S9 and Table S2. We found that the overall compositional ratio of Pb:Sn: (I + Br) is close to 0.4:0.6:3 indicating the uniform distribution of all elements. Furthermore, the atomic ratios of Pb, Sn, I, and Br shown in Table S2 are almost similar to the stoichiometric composition of the precursors as $CsPb_{0.4}Sn_{0.6}I_3$, $CsPb_{0.4}Sn_{0.6}I_{2.7}Br_{0.3}$, $CsPb_{0.4}Sn_{0.6}I_{2.4}Br_{0.6}$, and $CsPb_{0.4}Sn_{0.6}I_2Br$ for $y = 0$, $y = 0.3$, $y = 0.6$, and $y = 1.0$, respectively. The slighly Sn-rich content (>0.6) could be attributed to SnF_2 additive for suppressing oxidation of Sn-based perovskites.

Next, we examined the photophysical properties of the $CsPb_{0.4}Sn_{0.6}I_{3-y}Br_y$ perovskite films. Fig. 4a shows the absorbance measured using a UV–vis spectrometer. The control ($CsPb_{0.4}Sn_{0.6}I_3$) shows wide absorption in NIR wavelengths exceeding 950 nm compared to conventional $CsPbI_3$ (710 nm) [12], confirming the decreased bandgap when the amount of Sn exceeds Pb (>50%). On the other hand,

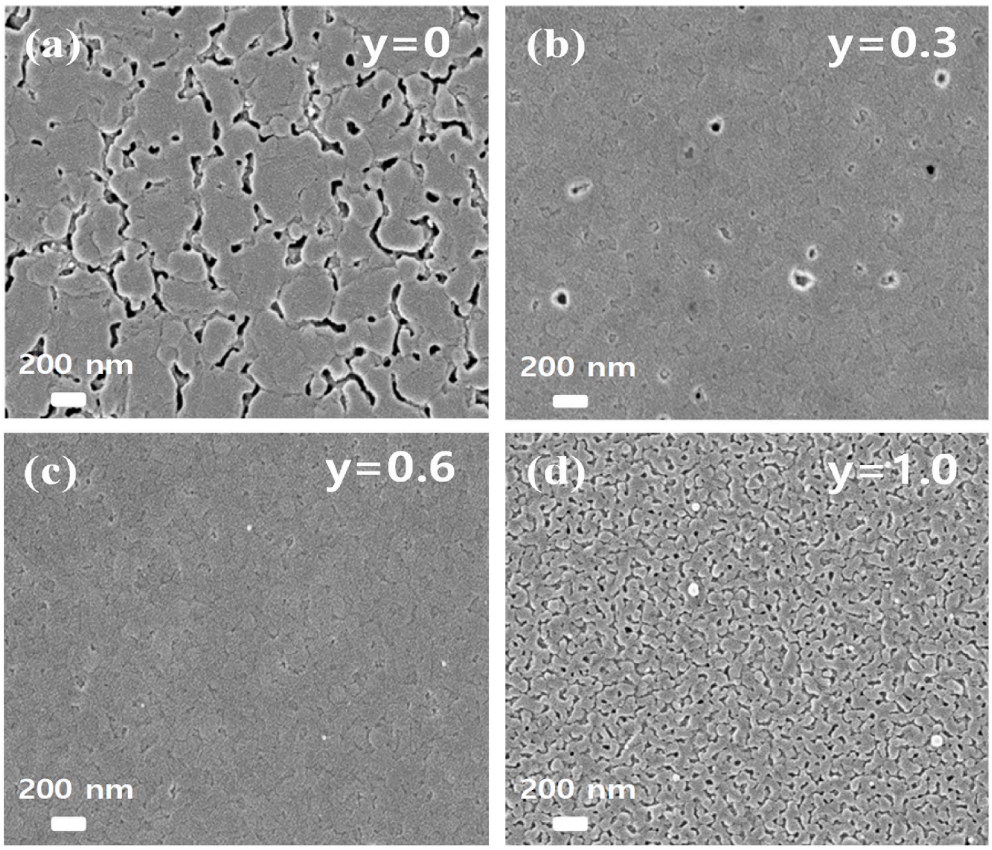

Fig. 3. SEM images of the inorganic Sn-rich $CsPb_{0.4}Sn_{0.6}I_{3-y}Br_y$ perovskite films with various Br contents: (a) $CsPb_{0.4}Sn_{0.6}I_3$, (b) $CsPb_{0.4}Sn_{0.6}I_{2.7}Br_{0.3}$, (c) $CsPb_{0.4}Sn_{0.6}I_{2.4}Br_{0.6}$, and (d) $CsPb_{0.4}Sn_{0.6}I_2Br$.

the addition of Br to the inorganic Sn-rich $CsPb_{0.4}Sn_{0.6}I_{3-y}Br_y$ perovskites causes the bandgap to increase, which should lead to a blueshift in the absorption spectrum. For clarity, we added an enlarged spectral range around 900 nm near the bandgap, as attached in inset of Fig. 4a. The addition of Br to the inorganic Sn-rich $CsPb_{0.4}Sn_{0.6}I_{3-y}Br_y$ perovskites tunes its bandgap to increase, which should lead to a blueshift in the absorption spectrum. The results are consistent with Fig. 4b. The Tauc plot in Fig. 4b shows the bandgap of the $CsPb_{0.4}Sn_{0.6}I_{3-y}Br_y$ perovskite films. This result is consistent with the trend of calculated bandgaps for different y values in Fig. S7b. The bandgap increased as the ratio of Br increased according to the absorbance data. The bandgaps of the $CsPb_{0.4}Sn_{0.6}I_{3-y}Br_y$ perovskites are 1.30, 1.33, 1.35, and 1.42 eV for $y = 0$, 0.3, 0.6, and 1.0, respectively. These bandgaps are much narrower than those of inorganic Pb–Sn perovskites (1.64–1.79 eV) reported to date [48,49], which can be essential for NIR absorption in perovskite-perovskite tandem photovoltaics. Fig. 4c shows the steady-state photoluminescence (SS-PL) of the inorganic Sn-rich $CsPb_{0.4}Sn_{0.6}I_{3-y}Br_y$ perovskite films. As the amount of Br increases, the peak SS-PL emission is shifted to shorter wavelengths (954, 931, 913, and 869 nm), in good agreement with the bandgap values in Fig. 4b. We also obtained FWHM in the SS-PL peak via Gaussian fitting (Fig. S10) [50,51]. As more Br is incorporated, the FWHM value decreases slightly from 88 nm at $y = 0$–83 nm at $y = 0.6$, indicating better crystallinity and fewer defect that are in good agreement with our XRD and SEM measurement results. In comparison, the FWHM value of $CsPb_{0.4}Sn_{0.6}I_2Br$ ($y = 1.0$) perovskite is much higher (122 nm) compared to other perovskites, also closely matching the XRD and SEM results. This indicates an increased amount of crystal defects that would enhance the non-radiative recombination paths. Furthermore, excess Br may cause light-induced phase separation [47]. This phase separation creates a high density of defects, which could be predicted by Urbach energy (E_u) calculated by $\alpha = \alpha_0 \exp(E/E_u)$, where α is the absorption coefficient from the absorbance spectra and $E = h\nu$ is the photon energy [52]. The values of E_u enabled us to evaluate the electronic disorders in the inorganic Sn-rich $CsPb_{0.4}Sn_{0.6}I_{3-y}Br_y$ perovskite films (Fig. S11a, b). $E_u = 0.36$, 0.33, 0.26, and 0.37 eV for $y = 0$, 0.3, 0.6, and 1.0, respectively. Obviously, the incorporation of Br lowered E_u to a minimum of 0.26 eV in $CsPb_{0.4}Sn_{0.6}I_{2.4}Br_{0.6}$ ($y = 0.6$) perovskite. In contrast, the $CsPb_{0.4}Sn_{0.6}I_2Br$ ($y = 1.0$) composition showed an increased E_u value indicating deterioration of electronic quality. These data also suggest that a Br ratio of $y = 0.6$ is desirable. The carrier lifetimes of $CsPb_{0.4}Sn_{0.6}I_{3-y}Br_y$ perovskite films were evaluated with time-resolved photoluminescence (TR-PL) in Fig. 4d and Table 1. The carrier lifetime of $CsPb_{0.4}Sn_{0.6}I_{2.4}Br_{0.6}$ (0.954 ns) was longer than those of other perovskites (0.284 ns for $y = 0.3$, 0.281 ns for $y = 1$). This is in good agreement with the results of SS-PL, XRD, and E_u analyses discussed above, and could be attributed to the reduced defect states and suppressed non-radiative recombination when there is a suitable amount of Br. The fabricated inorganic Sn-rich perovskite films were used as light absorbers in PSCs with ITO/PEDOT:PSS/$CsPb_{0.4}Sn_{0.6}I_{3-y}Br_y$/PCBM/$CeO_x$/Ag inverted structure (Fig. 5a). Poly(3, 4-ethylenedioxythiophene) polystyrenesulfonate (PEDOT:PSS) was treated with dimethyl sulfoxide (DMSO) to improve the device performance by increasing its conductivity as an HTL [53,54]. In addition, CeO_x interfacial layer was applied to improve the electron extraction and stability of device as a hole blocking layer [55]. The corresponding energy band diagram of the PSCs extracted from ultraviolet photoelectron spectroscopy (UPS, Fig. S12) data is shown in Fig. 5b. The addition of Br into the perovskite light absorber made the energy band alignment much favorable with HTL and ETL, leading to higher open circuit voltage (V_{oc}) values. Fig. 5c exhibits the J-V curves of the inorganic Sn-rich $CsPb_{0.4}Sn_{0.6}I_{3-y}Br_y$ PSCs. The corresponding photovoltaic

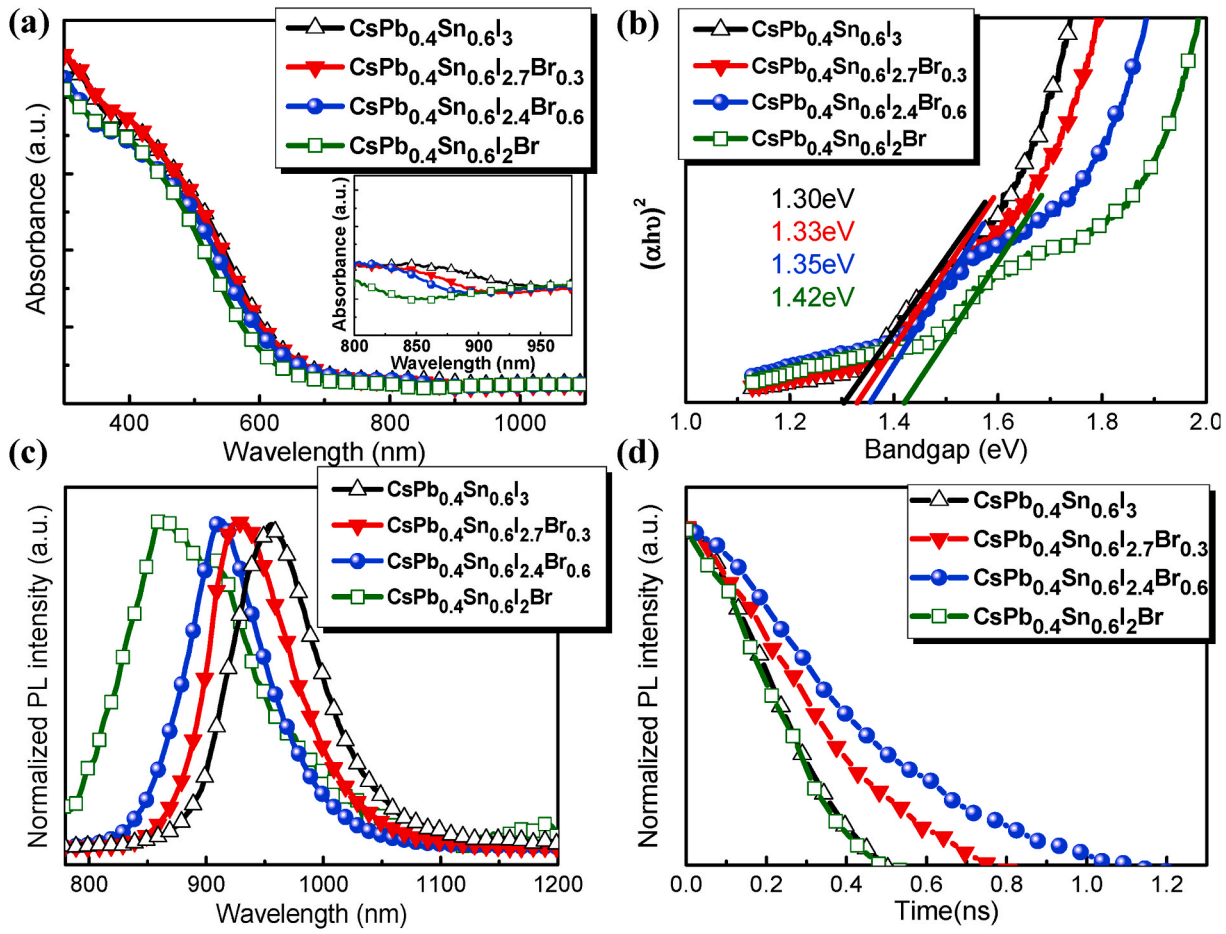

Fig. 4. (a) UV–vis absorption spectra with the inset of magnified absorbance edges, (b) Tauc plots, (c) steady-state photoluminescence (SS-PL), and (d) time-resolved photoluminescence (TR-PL) of the inorganic Sn-rich $CsPb_{0.4}Sn_{0.6}I_{3-y}Br_y$ perovskite films.

Table 1
TR-PL decay data of the inorganic Sn-rich $CsPb_{0.4}Sn_{0.6}I_{3-y}Br_y$ perovskite films.

Sample	A_1 (%)	τ_1 (ns)	A_2 (%)	τ_2 (ns)	τ_{ave} (ns)
$CsPb_{0.4}Sn_{0.6}I_3$	87.61	0.28	12.39	0.32	0.284
$CsPb_{0.4}Sn_{0.6}I_{2.7}Br_{0.3}$	72.14	0.60	27.86	0.72	0.635
$CsPb_{0.4}Sn_{0.6}I_{2.4}Br_{0.6}$	44.50	0.85	55.50	1.04	0.954
$CsPb_{0.4}Sn_{0.6}I_2Br$	55.43	0.31	44.57	0.25	0.281

parameters are shown in Table 2. For control, the inorganic Sn-rich PSC without Br (y = 0) has PCE = 7.04%, V_{oc} = 0.62 V, J_{sc} = 15.67 mA/cm^2, and FF = 0.723. On the other hand, the $CsPb_{0.4}Sn_{0.6}I_{2.4}Br_{0.6}$ (y = 0.6) PSC displayed PCE = 12.34%, V_{oc} = 0.86 V, J_{sc} = 19.02 mA/cm^2, and FF = 0.751. These values of PCE and V_{oc} are the highest among inorganic Sn-rich (Sn > 50%) PSCs reported to date. Furthermore, the V_{oc} loss ($E_g/q - V_{oc}$; E_g is the bandgap, q is the elementary charge) was only approximately 0.49 V, which is remarkably lower than other Sn-rich inorganic perovskites (0.99 V for $CsPb_{0.5}Sn_{0.5}IBr_2$, 1.3 V for $CsPb_{0.25}Sn_{0.75}IBr_2$) [49]. While maintaining a high FF value (0.751), a record PCE value was achieved in this study among inorganic Sn-rich (Sn > 50%) PSCs. The increased V_{oc} and FF can be ascribed to the wider bandgap, more favorable band alignment, and reduced defect or trap density in the perovskite film (Fig. 4c, d and Fig. S10, S11). In addition, the increase in J_{sc} can be attributed to the external quantum efficiency (EQE) spectra. In Fig. 5d, the wavelength range of the EQE spectrum is similar to the absorbance range. The integrated J_{sc} of the $CsPb_{0.4}Sn_{0.6}I_3$, $CsPb_{0.4}Sn_{0.6}I_{2.7}Br_{0.3}$, $CsPb_{0.4}Sn_{0.6}I_{2.4}Br_{0.6}$, and $CsPb_{0.4}Sn_{0.6}I_2Br$ PSCs is 14.89, 15.95, 18.05, and 14.15 mA/cm^2, respectively, which are not much different from the J_{sc} values by the solar simulator. The high EQE can imply an improved charge collection efficiency (i.e. reduced defects and longer lifetime) in $CsPb_{0.4}Sn_{0.6}I_{2.4}Br_{0.6}$, when we consider the similar absorption capability between $CsPb_{0.4}Sn_{0.6}I_3$ and $CsPb_{0.4}Sn_{0.6}I_{2.4}Br_{0.6}$ in Fig. 4a. These results prove the astonishing device performance of the inorganic Sn-rich $CsPb_{0.4}Sn_{0.6}I_{2.4}Br_{0.6}$ PSC. When it is compared to our preliminary study on $CsPbI_3$ (see Table S3) [12], the substantial improvement of device performance is observed (8.40% → 12.34%). The J_{sc} values integrated from EQE are 12.69 mA/cm^2 for $CsPbI_3$ and 18.05 mA/cm^2 for $CsPb_{0.4}Sn_{0.6}I_{2.4}Br_{0.6}$ PSCs. One of the huge differences is attributed to favorable coverage extension of EQE spectra (740 nm for $CsPbI_3$ and → 930 nm $CsPb_{0.4}Sn_{0.6}I_{2.4}Br_{0.6}$). On the contrary, at a higher Br concentration, $CsPb_{0.4}Sn_{0.6}I_2Br$ (y = 1.0) has a lower device performance due to the aforementioned discontinuous morphology, deteriorated PL properties, and higher E_u of the perovskite film. Fig. 5e shows the statistical distribution of PCE and good reproducibility of the enhancement in PCE. Fig. 5f shows the time evolution of PCE for the inorganic Sn-rich (Sn ≥ 50%) PSCs, which is also summarized in Table S4. Clearly, there is a scarcity of reports on inorganic Sn-rich (Sn ≥ 50%) PSCs, with only one study based on $CsPb_{0.25}Sn_{0.75}IBr_2$ having PCE = 3.13%. The PCE reported in this work is the highest among inorganic Sn-rich PSCs (Sn ≥ 50%), as shown in Fig. 5f and Table S4. We also conducted photo-stability test, as exhibited in Fig. S13, and the device showed an excellent photocurrent stability even it was measured in ambient air (at room temperature, R.H.:50%) without any encapsulation or protecting layer. Furthermore, very stable device operation (stabilized power conversion efficiency of 10.83%) was confirmed. It is noted here that there has never been such a stable output and high efficiency in

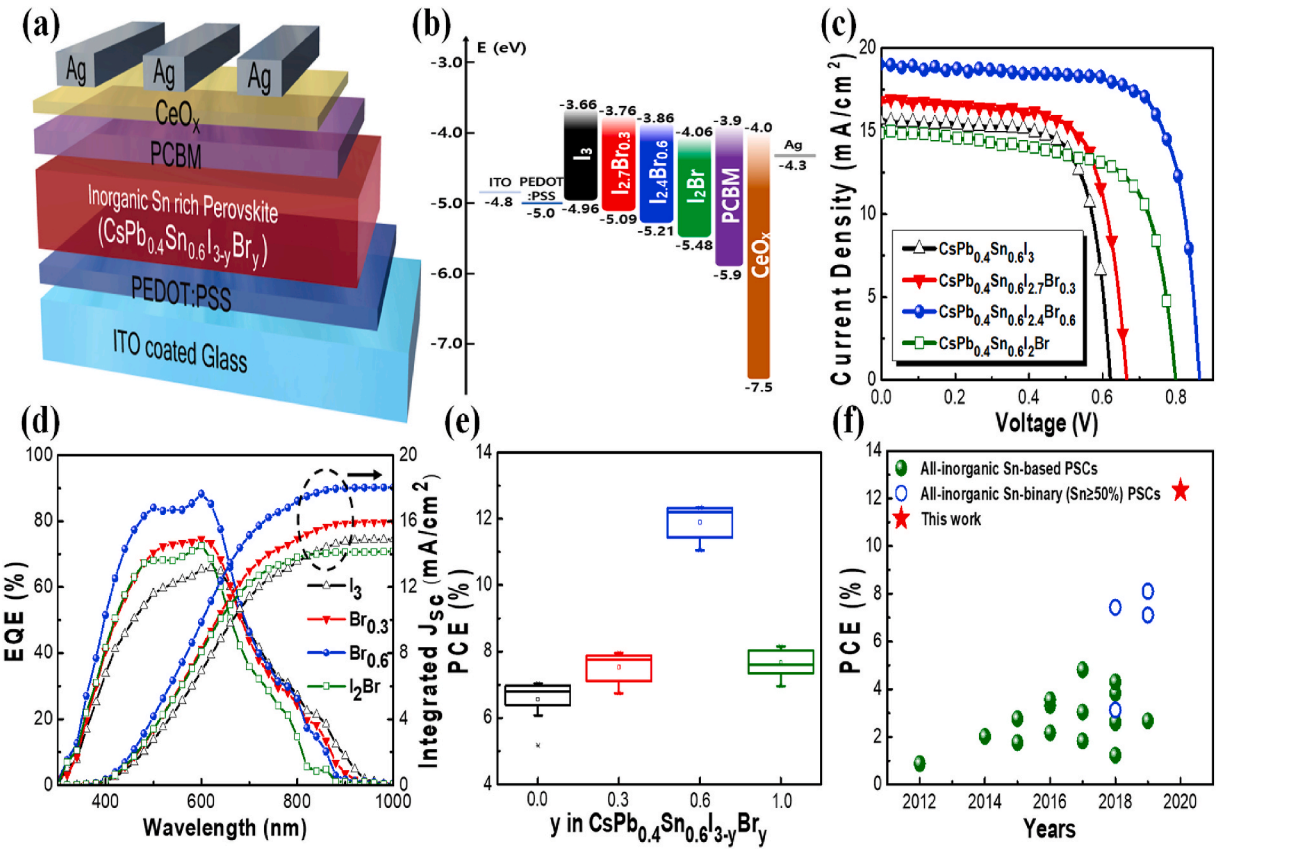

Fig. 5. (a) Schematic illustration of the inverted inorganic Sn-rich PSCs. (b) Energy band diagram of the fabricated $CsPb_{0.4}Sn_{0.6}I_{3-y}Br_y$ PSCs. (c) J-V characteristics of the best-performing $CsPb_{0.4}Sn_{0.6}I_{3-y}Br_y$ PSCs. (d) EQE spectra and the corresponding integrated J_{sc} curves of $CsPb_{0.4}Sn_{0.6}I_{3-y}Br_y$ PSCs with different Br contents. (e) Box chart showing statistical distribution in the PCE of $CsPb_{0.4}Sn_{0.6}I_{3-y}Br_y$ PSCs. (f) PCE distribution of the inorganic Sn-based and Sn-binary (Sn ≥ 50%) PSCs reported to date, including our work.

Table 2
Photovoltaic parameters of inorganic Sn-rich $CsPb_{0.4}Sn_{0.6}I_{3-y}Br_y$ PSCs under AM1.5 illumination.

Perovskites		Voc (V)	Jsc (mA/cm^2)	FF	PCE (%)
$CsPb_{0.4}Sn_{0.6}I_3$	Average	0.62 ± 0.006	15.58 ± 0.20	0.703 ± 0.022	6.79 ± 0.20
	Champion	0.62	15.67	0.723	7.04
$CsPb_{0.4}Sn_{0.6}I_{2.7}Br_{0.3}$	Average	0.64 ± 0.02	16.85 ± 0.21	0.687 ± 0.022	7.46 ± 0.52
	Champion	0.67	16.80	0.707	7.96
$CsPb_{0.4}Sn_{0.6}I_{2.4}Br_{0.6}$	Average	0.85 ± 0.01	18.88 ± 0.47	0.729 ± 0.014	11.67 ± 0.43
	Champion	0.86	19.02	0.751	12.34
$CsPb_{0.4}Sn_{0.6}I_2Br$	Average	0.80 ± 0.01	14.21 ± 0.65	0.681 ± 0.041	7.72 ± 0.36
	Champion	0.80	14.91	0.684	8.16

inorganic Sn-rich PSCs with narrow bandgap to date. In addition, we measured the long-term stability of the inorganic $CsPbI_3$, $CsPb_{0.4}Sn_{0.6}I_3$, and $CsPb_{0.4}Sn_{0.6}I_{2.4}Br_{0.6}$ PSCs without any encapsulation, under ambient air condition. In Fig. S14, the $CsPbI_3$ PSC without Sn was completely degraded within 12 h, and the parent compound $CsPb_{0.4}Sn_{0.6}I_3$ (y = 0) PSC without Br displayed a 50% reduction of the initial PCE within 5 days. In contrast, the $CsPb_{0.4}Sn_{0.6}I_{2.4}Br_{0.6}$ (y = 0.6) PSC showed remarkable ambient stability, maintaining about 70% of the initial efficiency for 30 days in air (RH: 30–70%) without any encapsulation. This stability is better than that of recent inorganic pristine $CsPbI_2Br$ (100% Pb-based) PSCs [56–58]. We also measured the thermal stability of our devices with different composition of perovskites for 18 h at elevated temperature of 65°C (Fig. S15). The representative $CsPbI_3$ PSC, pure-Pb perovskite, was completely degraded within 8 h because $CsPbI_3$ perovskite has severe instability, as already monitored in above XRD, UV–Vis absorption, and PL studies in addition to DFT calculation (Fig. 1a). With Sn 60% incorporation, on the other hand, all Pb–Sn perovskite films showcased better thermal stability than pristine pure-Pb perovskite, $CsPbI_3$ PSC. The best device (Br = 0.6) was maintained about 75% of initial efficiency after thermal treatment and it showcased the best stability compared to other compositions including representative inorganic $CsPbI_3$ perovskite, which is also consistent with the result from the structural stability estimation by DFT calculation and various film stability tests confirmed above. The stability of our the best device (Br = 0.6) was also compared to the $CsPbBr_3$ PSC which is well known for having excellent stability (Fig. S16). It showed a good long-term stability, showing a similar stability with the $CsPbBr_3$ device for about 15 days. After that, $CsPbBr_3$ showcased better stability, which can be attributed to pure Pb, and pure Br at B- and X-sites of ABX_3 that are much stable than Sn- and I- rich counterparts, respectively. Furthermore, X-ray photoelectron spectroscopy (XPS) was used to further analyze the stability of $CsPb_{0.4}Sn_{0.6}I_{3-y}Br_y$ perovskite films (y = 0, 0.6), as shown in Fig. S17. At y = 0, there are only two Sn 3d peaks (487.23 and 495.65 eV) assigned to Sn 3d5/2 and Sn 3d3/2,

respectively. These peaks were shifted by 150 meV to higher binding energies of 487.38 and 495.80 eV after Br substitution (y = 0.6). This increased binding energy could imply that the content of Sn^{4+} is decreased by Br addition, which significantly enhances the air stability of perovskite films [59,60]. We also evaluated the effect of Br incorporation on the electrical properties of $CsPb_{0.4}Sn_{0.6}I_{3-y}Br_y$ perovskite films by measuring the Hall effect. Hall measurement results are given by averaging each measurement tested on making three samples each for $CsPb_{0.4}Sn_{0.6}I_3$ and $CsPb_{0.4}Sn_{0.6}I_{2.4}Br_{0.6}$ in Table S5. As shown in Table S5, the average hole concentration of $CsPb_{0.4}Sn_{0.6}I_{2.4}Br_{0.6}$ (y = 0.6) perovskite film is (4.01 ± 0.074) × 10^{14} cm^{-3}, which is ~2.5% lower than that for pristine $CsPb_{0.4}Sn_{0.6}I_3$ (y = 0) perovskite at (4.1 ± 0.13) × 10^{14} cm^{-3}. It has been reported that the easy oxidation of Sn^{2+} to Sn^{4+} facilitates the formation of Sn vacancies, which increases the hole density [59]. However, in our case, the reduced hole density of $CsPb_{0.4}Sn_{0.6}I_{2.4}Br_{0.6}$ indicates that the oxidation of Sn^{2+} to Sn^{4+} is suppressed by Br addition, which is in good agreement with our XPS analysis. It is speculated that, when the Pb–Sn perovskites incorporating Br are annealed at above 60 °C, the Br atoms escape from the perovskite crystal lattice due to a higher vapor pressure than I, forming defect states related to the halide vacancy [61]. These halide vacancy levels are located near the CBM, acting as shallow donors that reduce the hole density [47]. Therefore, the above XPS and Hall effect measurements revealed that the incorporation of Br reduced the Sn vacancy, which contributed to the air stability of the inorganic Sn-rich $CsPb_{0.4}Sn_{0.6}I_{3-y}Br_y$ PSC at y = 0.6. Additionally, the hole mobility (μ) of the parent compound $CsPb_{0.4}Sn_{0.6}I_3$ is (2.21 ± 0.93) × 10^2 cm^2 V^{-1} s^{-1} whereas that of $CsPb_{0.4}Sn_{0.6}I_{2.4}Br_{0.6}$ is (7.23 ± 7.94) × 10^2 cm^2 V^{-1} s^{-1}, presumably due to the enhanced crystallinity as confirmed by DFT study and XRD analyses mentioned above. The high hole mobility in the $CsPb_{0.4}Sn_{0.6}I_{2.4}Br_{0.6}$ perovskite film would be beneficial for carrier injection to the HTL and improving J_{sc} in the PSCs. To explain the high PCE of $CsPb_{0.4}Sn_{0.6}I_{2.4}Br_{0.6}$ PSC, electrochemical impedance spectroscopy (EIS) and light intensity-dependent measurements of J_{sc} and V_{oc} were performed. Fig. 6a shows EIS data for the $CsPb_{0.4}Sn_{0.6}I_3$ (y = 0) and $CsPb_{0.4}Sn_{0.6}I_{2.4}Br_{0.6}$ (y = 0.6) devices measured in the dark within the frequency range from 1 kHz to 1 MHz [62]. The spectrum shows arcs fitted to the equivalent circuit consisting of series, parallel resistances, and a parallel capacitance (inset of Fig. 6a). The parallel resistance is the recombination resistance (R_{rec}), which increased from 4.88 × 10^4 to 2.85 × 10^5 Ω when y increased from 0 to 0.6. Thus, the EIS result reveals that the $CsPb_{0.4}Sn_{0.6}I_{2.4}Br_{0.6}$ perovskite with much higher R_{rec} has much lower recombination loss than $CsPb_{0.4}Sn_{0.6}I_3$ (y = 0), because the two devices used the same materials except for the light absorber. This analysis can explain the high V_{oc} values mentioned above. Serial resistance was also extracted, showing a slight decrease from 40.1 to 39.2 Ω with Br addition. The light intensity dependence of J_{sc} in Fig. 6b indicated a steeper slope (0.983) in $CsPb_{0.4}Sn_{0.6}I_{2.4}Br_{0.6}$ than in $CsPb_{0.4}Sn_{0.6}I_3$ (0.949). Thus, the non-radiative, trap-assisted recombination was reduced after Br was added into the parent compound $CsPb_{0.4}Sn_{0.6}I_3$. In other words, the incorporated Br helped passivate defect states in the perovskite films, resulting in an effective improvement in the device performance. To analyze the recombination kinetics, the light intensity-dependent V_{oc} data are plotted in Fig. 6c. The relationship between V_{oc} and light intensity (I) is $V_{oc} = (nkT/q)\ln(I/I_o + 1)$, where n is the ideality factor, q is the elementary charge, k is the Boltzmann constant, and T is the temperature [41]. It is known that n approaches unity when the bimolecular recombination is dominant, whereas it approaches 2 when trap-assisted Shockley-Read-Hall (SRH) recombination is dominant. The n value of $CsPb_{0.4}Sn_{0.6}I_3$ (y = 0) device is 1.85, and thus it is dominated by trap-assisted SRH recombination. The addition of Br reduced n to 1.56 in the $CsPb_{0.4}Sn_{0.6}I_{2.4}Br_{0.6}$ (y = 0.6) device, suggesting a suppressed SRH recombination. This value is higher than that of organic cation-$MASn_{0.6}Pb_{0.4}I_{2.6}Br_{0.4}$ in our previous work (n = 1.17, indicating dominant bimolecular recombination) [41]. This might be one of the clues why the PCE of the inorganic PSCs is lower

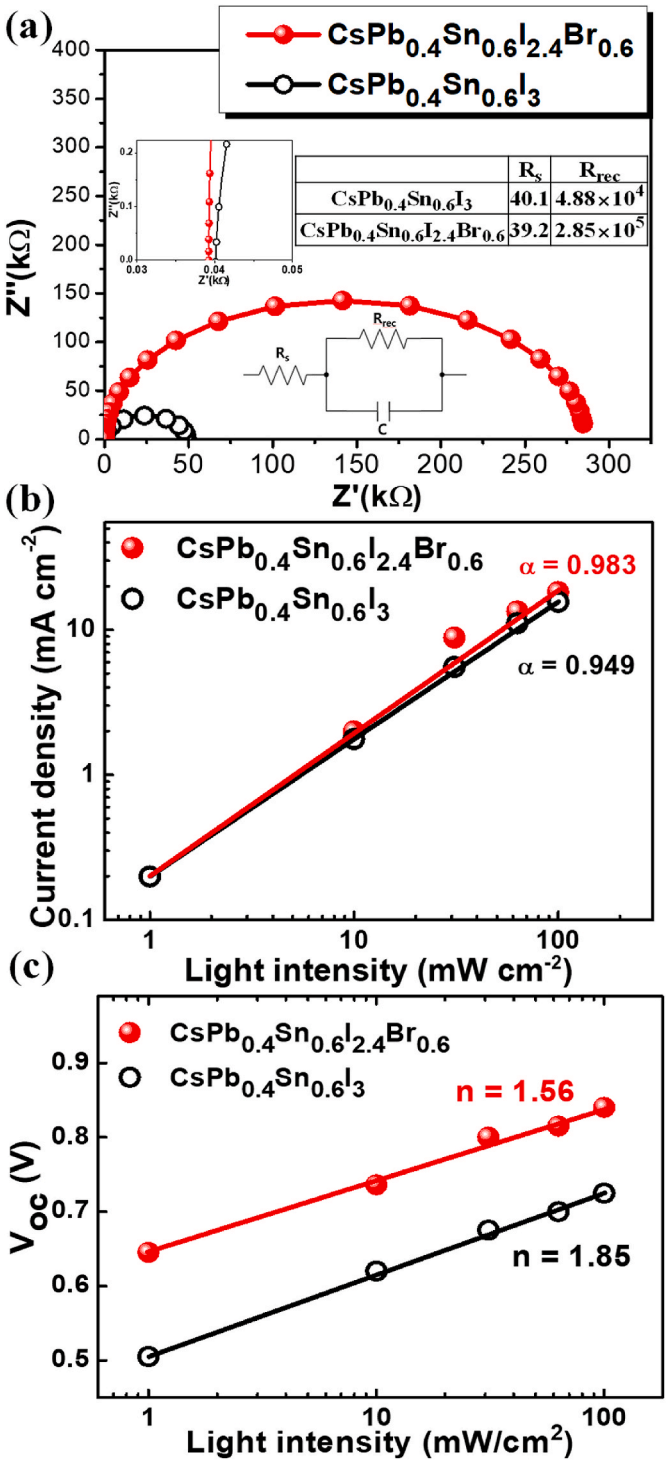

Fig. 6. (a) Nyquist plots of $CsPb_{0.4}Sn_{0.6}I_3$ and $CsPb_{0.4}Sn_{0.6}I_{2.4}Br_{0.6}$ PSCs. Inset: the equivalent circuit, the enlarged high-frequency region, and the table of simulated results. (b) Light intensity-dependent J_{sc} for $CsPb_{0.4}Sn_{0.6}I_3$ and $CsPb_{0.4}Sn_{0.6}I_{2.4}Br_{0.6}$ PSCs. (c) Light intensity-dependent V_{oc} for representative Sn-rich PSCs using $CsPb_{0.4}Sn_{0.6}I_3$, $CsPb_{0.4}Sn_{0.6}I_{2.4}Br_{0.6}$.

than that of OIH PSCs. From our results, the higher n value and insufficient tolerance factor (0.848) of the inorganic perovskite compared to OIH perovskite (0.956 for $MASn_{0.6}Pb_{0.4}I_{2.6}Br_{0.4}$) would be one reason limiting its performance. One possible solution is to increase the tolerance factor via compositional engineering for better structural stability [63,64]. For example, metal ions smaller than Sn^{2+} and Pb^{2+}, such as Sb^{3+} (0.76 Å), In^{3+} (0.80 Å), and Mn^{2+} (0.83 Å) can be utilized at the B

site of ABX_3 to achieve favorable tolerance factor in the inorganic Sn-rich perovskite film proposed in this work [65]. From our results, we are convinced that the $CsPb_{0.4}Sn_{0.6}I_{2.4}Br_{0.6}$ PSC is the most advanced inorganic Pb–Sn binary perovskite reported to date, because it shows significant improvements in the essential aspects of durability, Pb reduction, performance, and narrow bandgap as required in recent perovskite photovoltaic technology.

4. Conclusions

We demonstrated novel Pb–Sn binary mixed halide inorganic perovskites ($CsPb_{1-x}Sn_xI_{3-y}Br_y$) with suitable bandgaps in the range of 1.30–1.42 eV for use in the inorganic Sn-rich PSCs. First, our simulation and experimental work indicated that 60% Pb substitution by Sn ($CsPb_{0.4}Sn_{0.6}I_3$) was effective for suppressing the phase instability and reducing the unfavorable wide bandgap of $CsPbI_3$ perovskites. After a proper amount of Br was incorporated, a much more compact morphology and improved crystallinity were observed in the $CsPb_{0.4}Sn_{0.6}I_{2.4}Br_{0.6}$ perovskite film, which also displayed a desirable narrow bandgap of 1.35 eV. In addition, there were fewer defect-induced carrier recombination centers, and a longer carrier lifetime was achieved after mixed halide modification of the parent compound $CsPb_{0.4}Sn_{0.6}I_3$. Furthermore, the trap-assisted recombination was significantly suppressed in $CsPb_{0.4}Sn_{0.6}I_{2.4}Br_{0.6}$ with the addition of Br. As a result, the PCE of the PSC was drastically enhanced from 7.04% for $CsPb_{0.4}Sn_{0.6}I_3$ to 12.34% for $CsPb_{0.4}Sn_{0.6}I_{2.4}Br_{0.6}$, with a high V_{oc} of 0.86 V. The PCE and V_{oc} are the highest values among inorganic Sn-rich (Sn > 50%) PSCs reported to date. The unencapsulated $CsPb_{0.4}Sn_{0.6}I_{2.4}Br_{0.6}$ PSC showed remarkable long-term stability by retaining more than 70% of the initial efficiency for 30 days in ambient environment, surpassing the 100% Pb-based $CsPbI_3$ and $CsPbI_2Br$ PSCs. Also, remarkable thermal and photostability of the device were demonstrated. These remarkable results will be very important for developing highly efficient, stable, and inorganic Pb–Sn narrow bandgap PSCs, as well as their application in perovskite tandem solar cells.

CRediT authorship contribution statement

Seojun Lee: Methodology, Investigation, Data curation, Writing - original draft. **Janghyuk Moon:** Software, Validation, Writing - original draft. **Jun Ryu:** Methodology, Validation, Formal analysis. **Bhaskar Parida:** Data curation, Visualization. **Saemon Yoon:** Methodology, Investigation, Data curation. **Dong-Gun Lee:** Investigation, Data curation. **Jung Sang Cho:** Visualization, Writing - review & editing, Funding acquisition. **Shuzi Hayase:** Writing - review & editing, Supervision. **Dong-Won Kang:** Conceptualization, Writing - review & editing, Supervision, Project administration, Funding acquisition.

Declaration of competing interest

The authors declare that they have no known competing financial interests or personal relationships that could have appeared to influence the work reported in this paper.

Acknowledgement

This work was supported by the National Research Foundation of Korea (NRF) grant funded by the Korea government (MSIT) (NRF-2018R1C1B6008028, 2019K2A9A2A08000132 and 2018R1A4A1024691) and also supported by Korea Institute of Energy Technology Evaluation and Planning(KETEP) grant funded by the Korea government (MOTIE) (20193091010160, Development of 3D eyed transparent inorganic photovoltaic module).

Appendix A. Supplementary data

Supplementary data to this article can be found online at https://doi.org/10.1016/j.nanoen.2020.105309.

References

[1] S. Guarnera, A. Abate, W. Zhang, J.M. Foster, G. Richardson, A. Petrozza, H. J. Snaith, Improving the long-term stability of perovskite solar cells with a porous Al_2O_3 buffer layer, J. Phys. Chem. Lett. 6 (2015) 432–437, https://doi.org/10.1021/jz502703p.

[2] N.K. Noel, S.D. Stranks, A. Abate, C. Wehrenfennig, S. Guarnera, A.-A. Haghighirad, A. Sadhanala, G.E. Eperon, S.K. Pathak, M.B. Johnston, A. Petrozza, L.M. Herz, H.J. Snaith, Lead-free organic–inorganic tin halide perovskites for photovoltaic applications, Energy Environ. Sci. 7 (2014) 3061–3068, https://doi.org/10.1039/C4EE01076K.

[3] W. Liao, D. Zhao, Y. Yu, C.R. Grice, C. Wang, A.J. Cimaroli, P. Schulz, W. Meng, K. Zhu, R.G. Xiong, Y. Yan, Lead-free inverted planar formamidinium tin triiodide perovskite solar cells achieving power conversion efficiencies up to 6.22%, Adv. Mater. 28 (2016) 9333–9340, https://doi.org/10.1002/adma.201602992.

[4] S. Öz, J.-C. Hebig, E. Jung, T. Singh, A. Lepcha, S. Olthof, F. Jan, Y. Gao, R. German, P.H. van Loosdrecht, K. Meerholz, T. Kirchartz, S. Mathur, Zero-dimensional $(CH_3NH_3)_3Bi_2I_9$ perovskite for optoelectronic applications, Sol. Energy Mater. Sol. Cells 158 (2016) 195–201, https://doi.org/10.1016/j.solmat.2016.01.035.

[5] M. Kulbak, S. Gupta, N. Kedem, I. Levine, T. Bendikov, G. Hodes, D. Cahen, Cesium enhances long-term stability of lead bromide perovskite-based solar cells, J. Phys. Chem. Lett. 7 (2016) 167–172, https://doi.org/10.1021/acs.jpclett.5b02597.

[6] W. Xiang, Z. Wang, D.J. Kubicki, W. Tress, J. Luo, D. Prochowicz, S. Akin, L. Emsley, J. Zhou, G. Dietler, M. Grätzel, A. Hagfeldt, Europium-doped $CsPbI_2Br$ for stable and highly efficient inorganic perovskite solar cells, Joule 3 (2019) 205–214, https://doi.org/10.1016/j.joule.2018.10.008.

[7] X. Liu, X. Tan, Z. Liu, H. Ye, B. Sun, T. Shi, Z. Tang, G. Liao, Boosting the efficiency of carbon-based planar $CsPbBr_3$ perovskite solar cells by a modified multistep spin-coating technique and interface engineering, Nanomater. Energy 56 (2019) 184–195, https://doi.org/10.1016/j.nanoen.2018.11.053.

[8] H. Yuan, Y. Zhao, J. Duan, Y. Wang, X. Yang, Q. Tang, All-inorganic $CsPbBr_3$ perovskite solar cell with 10.26% efficiency by spectra engineering, J. Mater. Chem. 6 (2018) 24324–24329, https://doi.org/10.1039/C8TA08900K.

[9] W. Zhu, Q. Zhang, C. Zhang, Z. Zhang, D. Chen, Z. Lin, J. Chang, J. Zhang, Y. Hao, Aged precursor solution toward low-temperature fabrication of efficient carbon-based all-inorganic planar $CsPbIBr_2$ perovskite solar cells, ACS Appl. Energy Mater. 1 (2018) 4991–4997, https://doi.org/10.1021/acsaem.8b00972.

[10] J.K. Nam, S.U. Chai, W. Cha, Y.J. Choi, W. Kim, M.S. Jung, J. Kwon, D. Kim, J. H. Park, Potassium incorporation for enhanced performance and stability of fully inorganic cesium lead halide perovskite solar cells, Nano Lett. 17 (2017) 2028–2033, https://doi.org/10.1021/acs.nanolett.7b00050.

[11] Z. Li, J. Xu, S. Zhou, B. Zhang, X. Liu, S. Dai, J. Yao, CsBr-induced stable $CsPbI_{3-x}Br_x$ (x< 1) perovskite films at low temperature for highly efficient planar heterojunction solar cells, ACS Appl. Mater. Interfaces 10 (2018) 38183–38192, https://doi.org/10.1021/acsami.8b11474.

[12] B. Parida, J. Ryu, S. Yoon, S. Lee, Y. Seo, J.S. Cho, D.-W. Kang, Two-step growth of $CsPbI_{3-x}Br_x$ films employing dynamic CsBr treatment: toward all-inorganic perovskite photovoltaics with enhanced stability, J. Mater. Chem. 7 (2019) 18488–18498, https://doi.org/10.1039/C9TA05948B.

[13] W. Shockley, H.J. Queisser, Detailed balance limit of efficiency of p-n junction solar cells, J. Appl. Phys. 32 (1961) 510–519, https://doi.org/10.1063/1.1736034.

[14] T.-B. Song, T. Yokoyama, C.C. Stoumpos, J. Logsdon, D.H. Cao, M.R. Wasielewski, S. Aramaki, M.G. Kanatzidis, Importance of reducing vapor atmosphere in the fabrication of tin-based perovskite solar cells, J. Am. Chem. Soc. 139 (2017) 836–842, https://doi.org/10.1021/jacs.6b10734.

[15] T.-B. Song, T. Yokoyama, S. Aramaki, M.G. Kanatzidis, Performance enhancement of lead-free tin-based perovskite solar cells with reducing atmosphere-assisted dispersible additive, ACS Energy Lett 2 (2017) 897–903, https://doi.org/10.1021/acsenergylett.7b00171.

[16] J.H. Heo, J. Kim, H. Kim, S.H. Moon, S.H. Im, K.-H. Hong, Roles of SnX_2 (X= F, Cl, Br) additives in tin-based halide perovskites toward highly efficient and stable lead-free perovskite solar cells, J. Phys. Chem. Lett. 9 (2018) 6024–6031, https://doi.org/10.1021/acs.jpclett.8b02555.

[17] T.-B. Song, T. Yokoyama, J. Logsdon, M.R. Wasielewski, S. Aramaki, M. G. Kanatzidis, Piperazine suppresses self-doping in $CsSnI_3$ perovskite solar cells, ACS Appl. Energy Mater. 1 (2018) 4221–4226, https://doi.org/10.1021/acsaem.8b00866.

[18] M. Chen, M.-G. Ju, H.F. Garces, A.D. Carl, L.K. Ono, Z. Hawash, Y. Zhang, T. Shen, Y. Qi, R.L. Grimm, D. Pacifici, X.C. Zeng, Y. Zhou, N.P. Padture, Highly stable and efficient all-inorganic lead-free perovskite solar cells with native-oxide passivation, Nat. Commun. 10 (2019) 1–8, https://doi.org/10.1038/s41467-018-07951-y.

[19] M. Hu, M. Chen, P. Guo, H. Zhou, J. Deng, Y. Yao, Y. Jiang, J. Gong, Z. Dai, Y. Zhou, F. Qian, X. Chong, J. Feng, R.D. Schaller, K. Zhu, N.P. Padture, Y. Zhou, Sub-1.4 eV bandgap inorganic perovskite solar cells with long-term stability, Nat. Commun. 11 (2020) 1–10, https://doi.org/10.1038/s41467-019-13908-6.

[20] H. Ban, Q. Sun, T. Zhang, H. Li, Y. Shen, M. Wang, Stabilization of inorganic $CsPb_{0.5}Sn_{0.5}I_2Br$ perovskite compounds by antioxidant tea polyphenol, Sol. RRL 4 (2019), 1900457, https://doi.org/10.1002/solr.201900457.

[21] P. Hohenberg, W. Kohn, Inhomogeneous electron gas, Phys. Rev. 136 (1964) B864, https://doi.org/10.1103/PhysRev.136.B864.

[22] G. Kresse, D. Joubert, From ultrasoft pseudopotentials to the projector augmented-wave method, Phys. Rev. B 59 (1999) 1758, https://doi.org/10.1103/PhysRevB.59.1758.

[23] G. Kresse, J. Furthmüller, Efficient iterative schemes for ab initio total-energy calculations using a plane-wave basis set, Phys. Rev. B 54 (1996) 11169, https://doi.org/10.1103/PhysRevB.54.11169.

[24] G. Kresse, J. Furthmüller, Efficiency of ab-initio total energy calculations for metals and semiconductors using a plane-wave basis set, Comput. Mater. Sci. 6 (1996) 15–50, https://doi.org/10.1016/0927-0256(96)00008-0.

[25] W. Tang, E. Sanville, G. Henkelman, A grid-based Bader analysis algorithm without lattice bias, J. Phys. Condens. Matter 21 (2009), 084204, https://doi.org/10.1088/0953-8984/21/8/084204.

[26] Y. Wang, M.I. Dar, L.K. Ono, T. Zhang, M. Kan, Y. Li, L. Zhang, X. Wang, Y. Yang, X. Gao, Y. Qi, M. Grätzel, Y. Zhao, Thermodynamically stabilized β-$CsPbI_3$–based perovskite solar cells with efficiencies > 18%, Science 365 (2019) 591–595, https://doi.org/10.1126/science.aav8680.

[27] T. Zhang, M.I. Dar, G. Li, F. Xu, N. Guo, M. Grätzel, Y. Zhao, Bication lead iodide 2D perovskite component to stabilize inorganic α-$CsPbI_3$ perovskite phase for high-efficiency solar cells, Sci. Adv. 3 (2017), e1700841, https://doi.org/10.1126/sciadv.1700841.

[28] M. Saliba, T. Matsui, K. Domanski, J.-Y. Seo, A. Ummadisingu, S.M. Zakeeruddin, J.-P. Correa-Baena, W.R. Tress, A. Abate, A. Hagfeldt, M. Grätzel, Incorporation of rubidium cations into perovskite solar cells improves photovoltaic performance, Science 354 (2016) 206–209, https://doi.org/10.1126/science.aah5557.

[29] N.J. Jeon, J.H. Noh, W.S. Yang, Y.C. Kim, S. Ryu, J. Seo, S.I. Seok, Compositional engineering of perovskite materials for high-performance solar cells, Nature 517 (2015) 476–480, https://doi.org/10.1038/nature14133.

[30] K. Yamamoto, S. Iikubo, J. Yamasaki, Y. Ogomi, S. Hayase, Structural stability of iodide perovskite: a combined cluster expansion method and first-principles study, J. Phys. Chem. C 121 (2017) 27797–27804, https://doi.org/10.1021/acs.jpcc.7b07910.

[31] W.-J. Yin, Y. Yan, S.-H. Wei, Anomalous alloy properties in mixed halide perovskites, J. Phys. Chem. Lett. 5 (2014) 3625–3631, https://doi.org/10.1021/jz501896w.

[32] R. Ali, G.J. Hou, Z.G. Zhu, Q.B. Yan, Q.R. Zheng, G. Su, Stable mixed group II (Ca, Sr) and XIV (Ge, Sn) lead-free perovskite solar cells, J. Mater. Chem. 6 (2018) 9220–9227, https://doi.org/10.1039/C8TA01490F.

[33] F. Liu, C. Ding, Y. Zhang, T.S. Ripolles, T. Kamisaka, T. Toyoda, S. Hayase, T. Minemoto, K. Yoshino, S. Dai, M. Yanagida, H. Noguchi, Q. Shen, Colloidal synthesis of air-stable Alloyed $CsSn_{1-x}Pb_xI_3$ perovskite nanocrystals for use in solar cells, J. Am. Chem. Soc. 139 (2017) 16708–16719, https://doi.org/10.1021/jacs.7b08628.

[34] H.-J. Feng, T.R. Paudel, E.Y. Tsymbal, X.C. Zeng, Tunable optical properties and charge separation in $CH_3NH_3Sn_xPb_{1-x}I_3/TiO_2$-based planar perovskites cells, J. Am. Chem. Soc. 137 (2015) 8227–8236, https://doi.org/10.1021/jacs.5b04015.

[35] Z. Fang, M. Shang, X. Hou, Y. Zheng, Z. Du, Z. Yang, K.-C. Chou, W. Yang, Z. L. Wang, Y. Yang, Bandgap alignment of α-$CsPbI_3$ perovskites with synergistically enhanced stability and optical performance via B-site minor doping, Nanomater. Energy 61 (2019) 389–396, https://doi.org/10.1016/j.nanoen.2019.04.084.

[36] Y. Hu, F. Bai, X. Liu, Q. Ji, X. Miao, T. Qiu, S. Zhang, Bismuth incorporation stabilized α-$CsPbI_3$ for fully inorganic perovskite solar cells, ACS Energy Lett 2 (2017) 2219–2227, https://doi.org/10.1021/acsenergylett.7b00508.

[37] Q. Wang, X. Zheng, Y. Deng, J. Zhao, Z. Chen, J. Huang, Stabilizing the α-phase of $CsPbI_3$ perovskite by sulfobetaine zwitterions in one-step spin-coating films, Joule 1 (2017) 371–382, https://doi.org/10.1016/j.joule.2017.07.017.

[38] C.F.J. Lau, X. Deng, J. Zheng, J. Kim, Z. Zhang, M. Zhang, J. Bing, B. Wilkinson, L. Hu, R. Patterson, S. Huang, A. Ho-Baillie, Enhanced performance via partial lead replacement with calcium for a $CsPbI_3$ perovskite solar cell exceeding 13% power conversion efficiency, J. Mater. Chem. 6 (2018) 5580–5586, https://doi.org/10.1039/C7TA11154A.

[39] K. Galkowski, A. Surrente, M. Baranowski, B. Zhao, Z. Yang, A. Sadhanala, S. Mackowski, S.D. Stranks, P. Plochocka, Excitonic properties of low-band-gap lead–tin halide perovskites, ACS Energy Lett 4 (2019) 615–621, https://doi.org/10.1021/acsenergylett.8b02243.

[40] Z. Yang, C.-C. Chueh, P.-W. Liang, M. Crump, F. Lin, Z. Zhu, A.K.-Y. Jen, Effects of formamidinium and bromide ion substitution in methylammonium lead triiodide toward high-performance perovskite solar cells, Nanomater. Energy 22 (2016) 328–337, https://doi.org/10.1016/j.nanoen.2016.02.033.

[41] S. Lee, D.-W. Kang, Highly efficient and stable Sn-rich perovskite solar cells by introducing bromine, ACS Appl. Mater. Interfaces 9 (2017) 22432–22439, https://doi.org/10.1021/acsami.7b04011.

[42] G. Chai, S. Luo, H. Zhou, W.A. Daoud, $CH_3NH_3PbI_{3-x}Br_x$ perovskite solar cells via spray assisted two-step deposition: impact of bromide on stability and cell performance, Mater. Des. 125 (2017) 222–229, https://doi.org/10.1016/j.matdes.2017.04.010.

[43] F. Ansari, M. Salavati-Niasari, P. Nazari, N. Mir, V. Ahmadi, B. Abdollahi Nejand, Long-term durability of bromide-incorporated perovskite solar cells via a modified vapor-assisted solution process, ACS Appl. Energy Mater. 1 (2018) 6018–6026, https://doi.org/10.1021/acsaem.8b01075.

[44] N. Wang, Y. Zhou, M.G. Ju, H.F. Garces, T. Ding, S. Pang, X.C. Zeng, N.P. Padture, X.W. Sun, Heterojunction-depleted lead-free perovskite solar cells with coarse-grained B-γ-$CsSnI_3$ thin films, Adv. Energy Mater. 6 (2016), 1601130, https://doi.org/10.1002/aenm.201601130.

[45] K. Marshall, M. Walker, R. Walton, R. Hatton, Enhanced stability and efficiency in hole-transport-layer-free $CsSnI_3$ perovskite photovoltaics, Nat. Energy 1 (2016) 1–9, https://doi.org/10.1038/nenergy.2016.178.

[46] D. Sabba, H.K. Mulmudi, R.R. Prabhakar, T. Krishnamoorthy, T. Baikie, P.P. Boix, S. Mhaisalkar, N. Mathews, Impact of anionic Br– substitution on open circuit voltage in lead free perovskite ($CsSnI_{3-x}Br_x$) solar cells, J. Phys. Chem. C 119 (2015) 1763–1767, https://doi.org/10.1021/jp5126624.

[47] C. Li, Z. Song, D. Zhao, C. Xiao, B. Subedi, N. Shrestha, M.M. Junda, C. Wang, C. S. Jiang, M. Al-Jassim, R.J. Ellingson, N.J. Podraza, K. Zhu, Y. Yan, Reducing saturation-current density to realize high-efficiency low-bandgap mixed tin–lead halide perovskite solar cells, Adv. Energy Mater. 9 (2019), 1803135, https://doi.org/10.1002/aenm.201803135.

[48] J. Liang, P. Zhao, C. Wang, Y. Wang, Y. Hu, G. Zhu, L. Ma, J. Liu, Z. Jin, $CsPb_{0.9}Sn_{0.1}IBr_2$ based all-inorganic perovskite solar cells with exceptional efficiency and stability, J. Am. Chem. Soc. 139 (2017) 14009–14012, https://doi.org/10.1021/jacs.7b07949.

[49] N. Li, Z. Zhu, J. Li, A.K.Y. Jen, L. Wang, Inorganic $CsPb_{1-x}Sn_xIBr_2$ for efficient wide-bandgap perovskite solar cells, Adv. Energy Mater. 8 (2018), 1800525, https://doi.org/10.1002/aenm.201800525.

[50] C. Fei, L. Guo, B. Li, R. Zhang, H. Fu, J. Tian, G. Cao, Controlled growth of textured perovskite films towards high performance solar cells, Nanomater. Energy 27 (2016) 17–26, https://doi.org/10.1016/j.nanoen.2016.06.041.

[51] Y. Wang, J. Li, Q. Li, W. Zhu, T. Yu, X. Chen, Y. Zhou, X. Wang, Z. Zou, PbI_2 heterogeneous-cap-induced crystallization for an efficient $CH_3NH_3PbI_3$ layer in perovskite solar cells, Chem. Commun. 53 (2017) 5032–5035, https://doi.org/10.1039/C7CC01573A.

[52] S. Lee, J.S. Cho, D.-W. Kang, Perovskite/polyethylene oxide composites: toward perovskite solar cells without anti-solvent treatment, Ceram. Int. 45 (2019) 23399–23405, https://doi.org/10.1016/j.ceramint.2019.08.042.

[53] Y. Xia, K. Sun, J. Chang, J. Ouyang, Effects of organic inorganic hybrid perovskite materials on the electronic properties and morphology of poly (3, 4-ethylene-dioxythiophene): poly (styrenesulfonate) and the photovoltaic performance of planar perovskite solar cells, J. Mater. Chem. 3 (2015) 15897–15904, https://doi.org/10.1039/C5TA03456F.

[54] X. Wang, G. Lu, M. Zhang, Y. Gao, Y. Liu, L. Zhou, Z. Lin, High performance planar structure perovskite solar cells using a solvent dripping treatment on hole transporting layer, Coatings 10 (2020) 127, https://doi.org/10.3390/coatings10020127.

[55] Z. Xing, S.-H. Li, B.-S. Wu, X. Wang, L.-Y. Wang, T. Wang, H.-R. Liu, M.-L. Zhang, D.-Q. Yun, L.-L. Deng, S.-Y. Xie, R.-B. Huang, L.-S. Zheng, Photovoltaic performance and stability of fullerene/cerium oxide double electron transport layer superior to single one in pin perovskite solar cells, J. Power Sources 389 (2018) 13–19, https://doi.org/10.1016/j.jpowsour.2018.03.079.

[56] Z. Wang, A.K. Baranwal, P. Zhang, G. Kapil, T. Ma, S. Hayase, Delocalized molecule surface electronic modification for enhanced performance and high environmental stability of $CsPbI_2Br$ perovskite solar cells, Nanomater. Energy 66 (2019), 104180, https://doi.org/10.1016/j.nanoen.2019.104180.

[57] Y. Guo, F. Zhao, J. Tao, J. Jiang, J. Zhang, J. Yang, Z. Hu, J. Chu, Efficient and hole-transporting-layer-free $CsPbI_2Br$ planar heterojunction perovskite solar cells through rubidium passivation, ChemSusChem 12 (2019) 983–989, https://doi.org/10.1002/cssc.201802690.

[58] S. Yang, H. Zhao, Y. Han, C. Duan, Z. Liu, S. Liu, Europium and acetate Co-doping strategy for developing stable and efficient $CsPbI_2Br$ perovskite solar cells, Small 15 (2019), 1904387, https://doi.org/10.1002/smll.201904387.

[59] Y. Ogomi, A. Morita, S. Tsukamoto, T. Saitho, N. Fujikawa, Q. Shen, T. Toyoda, K. Yoshino, S.S. Pandey, T. Ma, S. Hayase, $CH_3NH_3Sn_xPb_{(1-x)}I_3$ Perovskite solar cells covering up to 1060 nm, J. Phys. Chem. Lett. 5 (2014) 1004–1011, https://doi.org/10.1021/jz5002117.

[60] J. Yuan, B. Li, C. Hao, Study on cobalt doped tin based perovskite material with enhanced air stability, Mater. Sci. Semicond. Process. 57 (2017) 95–98, https://doi.org/10.1016/j.mssp.2016.09.029.

[61] W.-J. Yin, T. Shi, Y. Yan, Superior photovoltaic properties of lead halide perovskites: insights from first-principles theory, J. Phys. Chem. C 119 (2015) 5253–5264, https://doi.org/10.1021/jp512077m.

[62] Z. Guo, S. Teo, Z. Xu, C. Zhang, Y. Kamata, S. Hayase, T. Ma, Achievable high V_{oc} of carbon based all-inorganic $CsPbIBr_2$ perovskite solar cells through interface engineering, J. Mater. Chem. 7 (2019) 1227–1232, https://doi.org/10.1039/C8TA09838G.

[63] A.D. Jodlowski, C. Roldán-Carmona, G. Grancini, M. Salado, M. Ralaiarisoa, S. Ahmad, N. Koch, L. Camacho, G. De Miguel, M.K. Nazeeruddin, Large guanidinium cation mixed with methylammonium in lead iodide perovskites for 19% efficient solar cells, Nat. Energy 2 (2017) 972–979, https://doi.org/10.1038/s41560-017-0054-3.

[64] Q. Wang, F. Lin, C.-C. Chueh, T. Zhao, M. Eslamian, A.K.-Y. Jen, Enhancing efficiency of perovskite solar cells by reducing defects through imidazolium cation incorporation, Mater, Today Energy 7 (2018) 161–168, https://doi.org/10.1016/j.mtener.2017.09.007.

[65] H.W. Qiao, S. Yang, Y. Wang, X. Chen, T.Y. Wen, L.J. Tang, Q. Cheng, Y. Hou, H. Zhao, H.G. Yang, A gradient heterostructure based on tolerance factor in high-performance perovskite solar cells with 0.84 fill factor, Adv. Mater. 31 (2019), 1804217, https://doi.org/10.1002/adma.201804217.

Seojun Lee: received his B.S. in the department of solar & energy engineering at Cheongju University. He is currently a Ph. D. candidate in the department of energy systems engineering at Chung-Ang University, Republic of Korea after getting his M. S. degree in the same institute. He is interested in the study on narrow bandgap Pb–Sn binary and inorganic perovskite solar cells.

Janghyuk Moon: is an assistant professor of school of energy system engineering at Chung-Ang University. He received his B. S. and Ph.D. degree in mechanical aerospace engineering from Seoul National University. His research aims to develop multi-scale simulation method for energy materials.

Jun Ryu: received his B.S. in the department of solar & energy engineering at Cheongju University. He is currently the master's course in the department of energy systems engineering at Chung-Ang University, Republic of Korea. His research interest is development of inorganic perovskite solar cells as well as inorganic charge transport layers.

Bhaskar Parida: received his M.Sc. in Physics from Berhampur University, Berhampur, India in 2007 and Ph.D. degree in Engineering from Department of Mechanical Engineering, Chonbuk National University, Korea in 2014. After his Ph.D. he worked as a post-doctoral researcher in the department of Mechanical Engineering and Semiconductor Physics Research Center, Chonbuk National University.

Currently, he is a post-doctoral researcher with the School of Energy System Engineering, Chung-Ang University, Korea. His current research interests include the fabrications and characterization of silicon solar cells, perovskite solar cells and light emitting diodes.

Saemon Yoon: received his B.S. in the school of solar & energy engineering at Cheongju University. He is currently a Ph.D. candidate in the department of energy systems engineering at Chung-Ang University, Korea after getting his M.S. degree in the same institute. His research interest is Pb-free perovskite solar cell as well as efficient inorganic charge transport layers.

Dong-Gun Lee: received his B.S. in the school of energy systems engineering at Chung-Ang University. He is currently the master's course in the department of energy systems engineering at Chung-Ang University. His research interest is perovskite solar cell as well as efficient inorganic charge transport layers.

Jung Sang Cho: received his Ph. D. from interdisciplinary program for bioengineering, college of engineering, Seoul national university, Korea in 2013, and had post-doc experience at the department of materials science and engineering, Korea university, Korea (2014–2016). He is currently a professor at the department of engineering chemistry, chungbuk national university, Korea since 2016. His research group works on the development of nanostructured materials for the energy storage, sensor, catalyst, display, and biomaterials. For details please see the lab website: https://jjj777.wixsite.com/professor-cho/members.

Shuzi Hayase: received his Ph.D from the Osaka University in 1983 and started his career as a researcher at Toshiba R&D Center from 1978 to 2000. In 2001, he started his career as a professor at the Kyushu Institute of Technology (National Institute). Since 2009, he is the supervisor for the PRESTO project (Japan Science and Technology Agency (JST), "Photo-energy conversion systems and materials for the next generation solar cells" project). He was the former dean of the graduate school of life science and systems engineering, Kyushu Institute of Technology. From 2016 to 2018, he was the Executive Director, vice-President of Kyushu Institute of Technology. Since 2019, he was appointed as the research professor at the University of Electro-Communications. His research interest focuses on printable solar cells.

Dong-Won Kang: received his Ph. D. degree from school of electrical engineering and computer science, Seoul National University, Korea in 2013, and performed additional research as a post-doctoral fellow from the department of physical electronics, Tokyo Institute of Technology, Japan (2013–2014). After that, he worked as an assistant professor in the school of solar & energy engineering, Cheongju university (2015–2017). Since 2018, he has been working as an assistant professor in the department of energy systems engineering, Chung-Ang University, Korea.

His research group works on energy materials and optoelectronic devices including perovskites and metal-oxides.